J. Fluid Mech. (2001), *vol.* 444, *pp.* 117–149. Printed in the United Kingdom

Organized motions in a jet in crossflow

By A. RIVERO[1], J. A. FERRÉ[1] AND FRANCESC GIRALT[2]

[1]Departament d'Enginyeria Mecànica

[2]Departament d'Enginyeria Química Escola Técnica Superior d'Enginyeria Química (ETSEQ), Universitat Rovira Virgili, Ctra. de Salou s/n, 43006-Tarragona, Catalunya, Spain

(Received 27 June 2000 and in revised form 26 March 2001)

An experimental study to identify the structures present in a jet in crossflow has been carried out at a jet-to-crossflow velocity ratio $U/U_{cf} = 3.8$ and Reynolds number $Re = U_{cf}D/\nu = 6600$. The hot-wire velocity data measured with a rake of eight $\times$-wires at $x/D = 5$ and 15 and flow visualizations using planar laser-induced fluorescence (PLIF) confirm that the well-established pair of counter-rotating vortices is a feature of the mean field and that the upright, tornado-like or Fric's vortices that are shed to the leeward side of the jet are connected to the jet flow at the core. The counter-rotating vortex pair is strongly modulated by a coherent velocity field that, in fact, is as important as the mean velocity field. Three different structures – folded vortex rings, horseshoe vortices and handle-type structures – contribute to this coherent field. The new handle-like structures identified in the current study link the boundary layer vorticity with the counter-rotating vortex pair through the upright tornado-like vortices. They are responsible for the modulation and meandering of the counter-rotating vortex pair observed both in video recordings of visualizations and in the instantaneous velocity field. These results corroborate that the genesis of the dominant counter-rotating vortex pair strongly depends on the high pressure gradients that develop in the region near the jet exit, both inside and outside the nozzle.

1. Introduction

A jet in crossflow discharging from a ground-level source is a natural flow phenomenon. It is also a flow of engineering interest that appears in many industrial processing units. Examples of jets in crossflow issuing from ground-level or elevated sources can be found in aeronautics (V/STOL, turbine blade cooling, control in re-entering, control vector thrust), industry (chemical plants, fuel injection in engines, chimneys) and nature (strongly buoyant plumes in massive fires and oil towers). This free turbulent flow is the result of the complex, three-dimensional interaction between the jet and the crossflow stream. Of the several flow regions that can be identified, the boundary layer region at the plane wall where the jet is injected and the jet flow close to the pipe wall near the exit are the most important in the genesis and evolution of the coherent structures that develop downstream.

The jet quickly bends in the direction of the crossflow (see figure 1) just after exiting from the nozzle. Two mechanisms have been claimed in the literature to explain this deflection: the pressure gradient between the upstream (high) and downstream (low) flow over the wall at the jet exit; and the entrainment of the jet flow into the crossflow stream. A false or pseudo-wake, with an almost null deficit of momentum (Morton

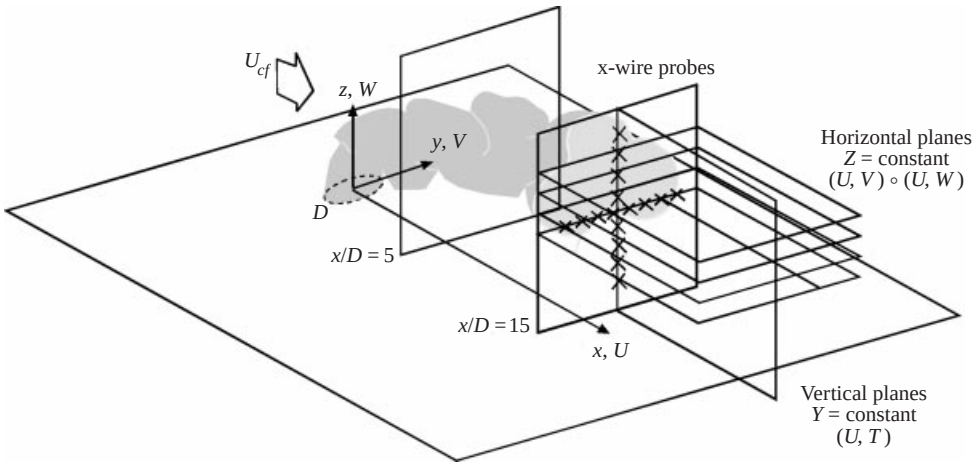

FIGURE 1. Experimental setup.

& Ibbetson 1996), develops downstream of the jet. Direct numerical simulations (DNS) and experiments have shown that alternate vortices are shed for Reynolds numbers in the range $500 \leqslant Re = U_{cf}D/\nu \leqslant 1000$ and jet-to-crossflow velocity ratio $VR = U/U_{cf} \approx 3$–4, in a way similar to the Kármán vortex street formed behind cylinders or solid bluff bodies (Fric & Roshko 1994; Rudman 1996; Kelso, Lim & Perry 1996; Morton & Ibbetson 1996; Yuan, Street & Ferziger 1999). Farther downstream, in the region where the jet flow becomes more parallel to the cross-stream, a pair of counter-rotating vortices appears. This counter-rotating vortex pair (CVP), which has attracted the attention of many researchers (Fearn & Weston 1978; Adler & Baron 1979; Broadwell & Breidenthal 1984; Karagozian 1986), is a strong feature of the flow that persists in the far field where the velocity defect of the jet is barely measurable (Pratte & Baines 1967). In fact, this feature appears even in the steady and laminar numerical calculations of the flow, and it seems to be qualitatively independent of the velocity ratio, the Reynolds number, and the shape of the nozzle.

There are several experimental studies reported in the literature dealing with the flow near the jet exit region and the effect of different devices on the penetration of the jet (Foss 1980; Andreopoulos 1985; Licinsky, True & Holderman 1995; Haven & Kurosaka 1997; Zaman & Foss 1997). Nevertheless, the detailed experimental study of this region is difficult and several numerical simulations, free of the experimental constraints, have been carried out. However, the boundary and initial conditions of most simulations are not very realistic. Some impose a top-hat velocity profile (Sykes, Lewellyn & Parker 1986; Rudman 1996) ignoring the influence of the external crossflow on the jet before its exit, which has been experimentally observed by Kelso *et al.* (1996) and Kelso & Smits (1995). Other calculations apply a zero-normal-velocity-derivative condition at the boundary wall instead of the standard no-slip condition (Coelho & Hunt 1989; Sykes *et al.* 1986). The numerical results obtained by Rivero (2000) with the commercial software package FLUENT reproduce the average streamline pattern of the CVP and compare reasonably well with the mean velocity profiles obtained by Yuan *et al.* (1999) with large-eddy simulations (LES) and with the experimental data for the pressure field over the wall reported by Margason (1993).

Most of the research done in this field before the 1990s was mainly focused on the

measurement of the mean statistical properties of the flow (Keffer & Baines 1963; Fearn & Weston 1978; Kamotani & Greber 1971; Schetz 1980). Little was known then about the non-stationary phenomena and the coherent structures of the jet, which are related to mixing and entrainment. More recently, attention has shifted towards the characterization of the organized large-eddy motions (coherent structures) of this flow by means of flow visualization, numerical simulation, and pattern recognition analysis of hot-wire data. The flow visualization studies include the visualization of the wake (Fric & Roshko 1994) and of the CVP (Morton & Ibbetson 1996; Blanchard, Brunet & Merlen 1999). Rudman (1996) performed the first direct numerical simulation at a very low Reynolds number. More recently, Yuan *et al.* (1999) used LES to study turbulent flow conditions. Eiff, Kawall & Keffer (1995) and Eiff & Keffer (1997) used pattern recognition to study the coherent structures in a jet in crossflow issuing from an elevated source (stack). They showed that the wake behind the stack synchronizes with the pseudo-wake of the jet and that some sort of structural connection exists in the far field between the pseudo-wake and the jet core.

The large-scale structures observed in the near field are either similar to those formed in the shear layer of a round free jet under the Kelvin–Helmholtz instability, or to the horseshoe vortices formed at a cylinder–wall junction. The roll-up process of the shear layer in the jet in crossflow occurs both upstream and downstream of the jet (see for example Yuan *et al.* 1999). On the upstream side the evolution of the shear layer vortices is more evident, clearer and occurs over a larger time scale than on the downstream side. This is so because in the latter these vortices break down and the mixing processes are very fast, and the roll-up takes place within a couple of diameters. On the other hand, the horseshoe vortex system lying on the wall around the jet exit is quite similar to that formed around a cylinder–wall junction. Kelso *et al.* (1996) visualized the roll-up mechanism on the upstream side and the vortex breakdown on the downstream side of the horseshoe vortex. The vortex rings resulting from the roll-up process can be relevant to the mixing process in this flow because, as will be shown later in this paper, they survive in the far field as folded rings. Krothapalli, Lourenco & Buchlin (1990), Kelso & Smits (1995), Morton & Ibbeston (1996) and Rudman (1996) also studied the horseshoe vortex system and how it relates to the shear layer roll-up and the shedding of vortices in the wake. The importance of these structures stems from their connection with the so-called upright, zipper or tornado-like vortices in the wake. A clever manipulation of the upstream region of the jet could modify some of the characteristics of the wake, e.g. the Strouhal number or the size of the ascending vortices. Although it is possible that from the point of view of most practical applications the wake does not have as much interest as the CVP, there are some applications, such as film cooling on turbine blades, in which this ascending mechanism could be of interest.

The far-field structures that have received most of the attention of researchers are the pseudo-Kármán vortices and the counter-rotating pair of vortices. The latter has been the most studied structure, undoubtedly due to its robustness and ease of measurement since it appears in the mean velocity field. Therefore, there is a considerable amount of work on two-dimensional models of the jet in crossflow based on the existence of an advected CVP. All models seem to indicate that, irrespective of the velocity ratio, the Reynolds number or other parameters (shape of the nozzle, laminar or turbulent boundary layer, thickness of the boundary layer, etc.), the counter-rotating pair of vortices will be present because they are an essential feature of this flow. However, the instantaneous photographs or numerical simulations of the flow by Smith *et al.* (1993), Smith & Mungal (1998) and Yuan *et al.* (1999)

show that the symmetrical CVP is an artifact of the averaging process since the instantaneous velocity field does not contain a symmetrical vortex pair. In addition, Zaman & Foss (1997) and Smith & Mungal (1998) have found that, despite the accurate control of the experimental conditions, sometimes it is difficult to obtain a symmetrical mean velocity field in the far region. As a consequence, the current study examines whether the CVP is the result of the interaction or superposition of several individual structures at different stages of evolution.

The pseudo-wake behind the jet has been another focus of interest since the work of Fric (1990) and Fric & Roshko (1994). These authors used the smoke-wire technique to visualize a jet in crossflow in a wind tunnel and showed that fluid coming from the wall boundary layer, and shed regularly from the leeward side of the jet, can be detected in the wake as ascending vortices. They found no evidence that fluid coming from the jet was shed into the wake. Eiff *et al.* (1995) studied a thermally contaminated jet issuing from a stack using hot-wire anemometry. The spectral analysis of the temperature signals in the wake showed that hot fluid was present in the wake with an almost periodic organization. Some contradiction seems to exist between these results and those of Fric & Roshko (1994). Nevertheless, it should be noted that in air the diffusion of smoke ($Sc > 1$) is smaller than the diffusion of heat, which closely follows the diffusion of vorticity ($Pr \approx 1$).

The aim of the present work is to educe the hidden structures present in a jet in a crossflow and to resolve the instantaneous characteristics of the large-scale motions contributing to the average CVP. The structural analysis is made by pattern recognition of a velocity data measured with a rake of eight $\times$-wires located at $x/D = 5$ and $x/D = 15$. The repetitive but non-periodic velocity events extracted from these data at several horizontal planes of measurement allows the reconstruction of the typical three-dimensional coherent velocity field. Attention is centred not only on the previously reported folded rings (Kelso *et al.* 1996) and vertical horseshoe-type vortices (Eiff & Keffer 1997), but also on the structural origin of the CVP modulation or meandering shape along its trajectory. The connection between the wake and core of the jet motions, and the mean CVP itself, is also studied. This hot-wire anemometry information is complemented with visualizations of the flow made with planar laser induced fluorescence (PLIF). The next, § 2 presents the experimental apparatus and the technique used to analyse the hot-wire data. Section 3 presents and discusses the results obtained, and the final conclusions of this work are included in § 4.

2. Experimental facility and techniques

2.1. *Experimental set-up*

Measurements have been performed in the open-circuit wind tunnel of the Department of Chemical Engineering of the University Rovira Virgili of Tarragona, which allows the control of the velocity between 2.5 and 20 m s^{-1} with a background turbulence level below 0.3% and a non-uniformity of the velocity profile at the entrance of the test section below 1%. The length of the test section is 3 m and the cross-section is 0.6 $\times$ 0.6 m. The air jet was discharged from a pressurized reservoir through a circular shaped nozzle ($U = 20\,\mathrm{m\,s^{-1}}$) perpendicularly into the wind tunnel main stream ($U_{cf} = 5.3\,\mathrm{m\,s^{-1}}$). The discharge flow velocity was controlled by means of a micrometer-controlled variable-throat sonic orifice valve to maintain a jet-to-crossflow velocity ratio $VR = U/U_{cf} = 3.8$. The nozzle diameter was $D = 0.02$ m and the Reynolds number $Re = U_{cf}D/\nu = 6600$. At the nozzle exit the velocity had a

typical top-hat velocity profile, with less than 0.5% of background turbulence. More experimental details can be found in Rivero (2000).

To control accurately the characteristics of the laminar boundary layer that interacts with the jet, a 1 cm thick Plexiglas flat plate, 0.6 m wide and 0.9 m long, was placed in the test section of the wind tunnel, 8 cm above the bottom wall. The nozzle was centred 0.2 m downstream of the wedge of the flat plate. Separation at this leading edge was avoided by use of an adjustable flap located at the trailing edge of the flat plate. The thickness of the laminar boundary layer at 0.10 m from the wedge was 3.3 mm and 5.4 mm at 0.15 m. These values are larger than the corresponding Blasius boundary layer thicknesses (2.7 and 3.6 mm respectively) due to the small adverse pressure gradient caused by the equipment placed inside the wind tunnel and the flap itself (flow blockage). This gradient could be compensated by means of the trailing edge flap, but its inclination was adjusted to avoid separation at the leading edge of the flat plate rather than yielding a zero-pressure-gradient boundary layer.

The Cartesian coordinate system was centred at the jet exit, with x and U in the streamwise direction, y and V in the spanwise direction and z and W in the vertical direction, as shown in figure 1. All the physical lengths have been normalized with respect to D ($X = x/D$; $Y = y/D$; $Z = z/D$) and all fluctuating velocities with respect to $U_{nor} = 1\,\mathrm{m\,s^{-1}}$. This reference velocity scale has been chosen because it is approximately the maximum r.m.s. value attained by the three velocity components of the jet at $x/D = 5$.

Several experiments were carried out in the water tunnel of Tarragona using the PLIF technique to support and confirm some of the results obtained by hot-wire anemometry. The tunnel has a test section 0.25×0.25 m wide and 1.5 m long. The crossflow velocity was fixed at $0.27\,\mathrm{m\,s^{-1}}$ with a nozzle diameter $D = 0.01$ m so that the Reynolds number was reduced to 2700, compared to the 6600 value in the air experiments, to maintain the velocity ratio close to 4. Visualizations at selected planes of the flow were recorded with a video camera at the standard frame rate of $25\,\mathrm{images\,s^{-1}}$. Each image was recorded with the electronic shutter set for individual exposure times of 2 ms, which was enough to freeze the motion of the smallest eddies present near the nozzle exit.

2.2. *Experimental procedure*

Two-components of the instantaneous velocity vector (U and V or U and W) were measured at several horizontal planes, using a rake of eight $\times$-wire probes, and at the vertical centreplane with a rake of normal wires and temperature probes. The measurement points covered the nodes of a grid located at several (y, z) positions, all of them contained in a vertical plane, normal to the cross-stream flow, at $X = 5$ and 15, as shown in figure 1. Each voltage signal was low-pass filtered at 2000 Hz and amplified before being digitized at 5000 Hz by a 12-bit A/D converter. The recording time in the series of experiments #l and #2 carried out to check the symmetry of the mean flow was 90 s, while 30 s of data were recorded for the rest of experiments. Thus, the smallest temporal fluctuation measured was 0.5 ms (corresponding to the cut-off frequency of 2000 Hz), which, using the Taylor hypothesis, yields a spatial resolution of $\Delta x = 2.5$ mm ($\Delta X = 0.125$) in the streamwise direction. The resolution in the spanwise or vertical direction is imposed by the probe spacing or by its vertical displacement steps ($\Delta y = \Delta z = 15$ mm or $\Delta Y = \Delta Z = 0.75$).

Both the streamwise and the spanwise velocities and the streamwise and the vertical velocity components were measured with the rake of probes spanning a horizontal plane (series #l, #2, #3, #4 and #5) at different z positions, as shown in figure 1.

	Series #1	Series #2	Series #3	Series #4	Series #5	Series #6
Measuring plane	Horizontal	Horizontal	Horizontal	Horizontal	Horizontal	Vertical
Direction of rake displacement	Z	Z	Z	Z	Z	Y
Streamwise position	$X = 5$	$X = 5$	$X = 5$	$X = 15$	$X = 15$	$X = 5$
Probe spacing	$\Delta Y = 0.75$	$\Delta Y = 0.75$	$\Delta Y = 0.75$	$\Delta Y = 0.75$	$\Delta Y = 0.75$	$\Delta Z = 0.37$
Position of the first and last probes	$Y = -3.75, 1.5$	$Y = -1.5, 3.75$	$Y = -1.5, 3.75$	$Y = -1.5, 3.75$	$Y = -1.5, 3.75$	$Z = 0.75, 7.5$
Number of probes	8X	8X	8X	8X	8X	6N,5T
Measured variables	U, V	U, V	U, W	U, V	U, W	U, T

TABLE 1. Experimental conditions.

Experiments in series #6 were carried out with the rake of probes spanning a vertical plane and sensing the streamwise velocity component and temperature with alternate probes. All measurements were made at $X = 5$ and $X = 15$, where the mean flow is quite horizontal at the VR studied, and both the spanwise (V) and the vertical (W) velocity components are of the same order of magnitude. The jet mean flow streamlines are respectively inclined 15° and 8° with respect to the horizontal at $X = 5$ and 15. Errors in the ×-wire measurements of the streamwise r.m.s. fluctuations caused by the high turbulence intensities present in the jet near the exit are estimated to be 10% at $X = 5$ and 5% at $X = 15$ (Kawall, Shokr & Keffer 1983). Probe spacing and other experimental details are summarized in table 1.

A series of preliminary tests was carried out to determine the blockage effect of the probe supporting mechanism. Initially, the vertical positioning screw supporting the probes was located at the vertical centreplane of the tunnel, 15D downstream from the measuring edge of the hot-wire probes. However, the mean velocity profiles were not symmetrical with respect to the mid-plane $y = 0$, as was also observed in the experiments carried out by Zaman & Foss (1997) and Smith & Mungal (1998). To overcome this inconsistency the mean velocity profile was then measured with the positioning screw successively located further downstream from the probes at steps of 5D. A reasonable symmetrical velocity profile was obtained with the vertical positioning screw placed 40D downstream from the measurement position.

2.3. *Pattern-recognition technique*

The turbulent signals were analysed using the pattern-recognition technique described by Ferré & Giralt (1989) and Kopp, Ferré & Giralt (1997). The technique identifies the footprints left by the non-periodic, but repetitive, eddies when they are advected by the bulk flow through the probes. The recognition process consists in correlating all data windows of some specified length $\delta x = U_{conv}\delta t$ (the simpler choice for the convection velocity is $U_{conv} = U_{cf}$) with an initial template of equal dimension containing the coherent information. Those windows with correlation above a threshold value are selected and their ensemble average obtained. To make the result more independent of the choice of initial template, the procedure is successively iterated, using the ensemble average as the initial template in the next iteration, until the process converges.

The pattern recognition analysis (PR) applied to the signal (U, V, etc.) of a single probe can be explained in terms of the search for organization in an n-dimensional space, where each portion of the signal of length n (n consecutive samples of the time series of U, V, etc.) is a point in this phase space. When consecutive points are plotted in the phase space, they describe a trajectory in n dimensions. Therefore, each characteristic large-scale event in the signal appears as a repetitive path along the same region of the space. Probably, two events will never be identical, because the turbulent signals have small scale or high-frequency components, but the global dynamic behaviour of the large scale is expected to be the same. In this context, the ensemble average can be interpreted as the centroid of a cloud of points, i.e. the representative event for this class, and the iterated pattern recognition procedure as a direct-search clustering technique.

The velocity signals were first centred to zero by subtracting the mean value and then processed by the PR algorithms. As a consequence, the raw ensemble averages that are obtained by PR are the representative patterns of the coherent velocity fluctuations that repeatedly appear at random time intervals within the recorded signals. Therefore the counter-rotating vortex pair detected in the mean velocity field cannot appear as such in these ensemble averages. Rather, the ensemble averages

should show the instantaneous flow organization that rides over the CVP and that is not revealed by spectral analysis, because is not periodic, or does not survive a time-averaging process because it occurs randomly in space. This is equivalent to a triple decomposition (Hussain 1983), where each turbulent signal is decomposed into a mean field plus a coherent field, with a random noise or incoherent field riding over them,

$$\boldsymbol{V}(x_i,t) = \boldsymbol{V}_m(x_i) + \boldsymbol{V}_c(x_i,t) + \boldsymbol{V}_r(t), \tag{1}$$

where $x_i = [x, y, z]$ and vectors are indicated by bold face. Because the autocorrelation of any turbulent signal decays to zero for $t > k\tau$, where τ is the integral scale of the turbulence, $\boldsymbol{V}_c(x_i,t)$ at any location x_i should be zero for $t > k\tau$, i.e. it has a limited time span. In this case, the CVP is contained in $\boldsymbol{V}_m(x_i)$ and the ensemble averages that are presented later are the limited-time-span coherent field, while $\boldsymbol{V}_r(t)$ accounts for the differences between the individual realizations contributing to an ensemble average. This coherent field $\boldsymbol{V}_c(x_i,t)$, obtained as the ensemble average of velocity fluctuations, does not coincide with the organization of the flow that would be captured by a camera moving along the flow at some selected convection velocity, U_{conv}. The decomposition that should be applied to the turbulent signals in this case is

$$\boldsymbol{V}(x_i,t) = U_{conv}\boldsymbol{e}_x + \boldsymbol{V}'_c(x_i,t) + \boldsymbol{V}'_r(t), \tag{2}$$

where the ensemble average of camera frames is $\boldsymbol{V}'_c(x_i,t)$. This decomposition (2) is related to equation (1) through expression

$$\boldsymbol{V}'_c(x_i,t) = \boldsymbol{V}_c(x_i,t) + \boldsymbol{V}_m(x_i) - U_{conv}\boldsymbol{e}_x. \tag{3}$$

Once $\boldsymbol{V}_c(x_i,t)$, the pattern recognition ensemble average, and $\boldsymbol{V}_m(x_i)$, the mean velocity profile, are known, $\boldsymbol{V}'_c(x_i,t)$, the camera ensemble average, can be obtained by first adding the mean velocity profile, $\boldsymbol{V}_m(x_i)$, to the pattern recognition ensemble average and then subtracting the convection velocity U_{conv}. Some of the initial results in the following sections correspond to horizontal z-plane measurements and are presented as vector maps $\boldsymbol{V}_c(y,t)$ in these z-planes using the triple decomposition, while the final results are presented as $\boldsymbol{V}'_c(y,t)$ using the double decomposition. From the point of view of analysing the raw velocity vectors, the difference between $\boldsymbol{V}_c(y,t)$ and $\boldsymbol{V}'_c(y,t)$ is not as important as when the raw velocity data contained in the ensemble averages, $\boldsymbol{V}_c(y,t)$ or $\boldsymbol{V}'_c(y,t)$, are transformed into coherent vorticity:

$$\boldsymbol{\Omega}_c = \nabla \times \boldsymbol{V}_c, \tag{4}$$

$$\boldsymbol{\Omega}'_c = \nabla \times \boldsymbol{V}'_c. \tag{5}$$

This is so because the mean velocity profile $\boldsymbol{V}_m(y)$ at any z-plane produces both a mean shear field and a mean vorticity field $\boldsymbol{\Omega}_m = \nabla \times \boldsymbol{V}_m$, that are contained in (5) but not in equation (4) since $\boldsymbol{\Omega}_c + \boldsymbol{\Omega}_m = \boldsymbol{\Omega}'_c$.

The last question concerning the PR results presented in this paper is related to the three-dimensional reconstruction of the flow from the two-dimensional slices summarized in table 1. Effectively, the rake of probes spans only one physical direction (y or z), while the time coordinate with the Taylor hypothesis provides the second 'physical' coordinate. Each ensemble average is, thus, a horizontal or vertical slice through the three-dimensional coherent structure. Several slices of the experimental data measured in consecutive horizontal planes, from close to the bottom boundary layer up to the top jet–crossflow interface, have been analysed consecutively and conditionally combined to yield a three-dimensional view of the structures. The

final ensemble average obtained in a plane is used as the initial template for the next plane. It should be taken into account that consecutive planes are only $0.75D$ apart and, therefore, the large-scale structures, with size of a few D, must leave simultaneous footprints in several planes. It would had been more accurate to follow the procedure described in Vernet *et al.* (1999), where a rake of a few probes located at a given position provided the reference information to conditionally sample the data measured by another rake of probes that swept the two-dimensional region of interest. The present procedure is simpler and still accurate enough, as it yields a reconstructed velocity map in the vertical plane from several successive horizontal plane measurements that is in agreement with simultaneously measured vertical-plane velocity patterns. This comparison is presented in § 3.

3. Results and discussion

3.1. *Mean and fluctuating velocity fields*

First, the symmetry of the jet in crossflow was checked with 90 s of recorded data (series #l and #2 in table 1) at $x = 5D$. Figures 2(*a*) and 2(*b*) show the mean velocity profiles of the U- and V-components of the velocity vector on both sides of the vertical centre plane ($y = 0$). The data are plotted as isocountours of the measured quantity, and the iso-level values are in $\mathrm{m\,s^{-1}}$. The mean velocity fields plotted in figure 2 are at least as consistently symmetrical, both in shape and magnitude, as those reported in previous studies (Smith *et al.* 1993; Licinsky *et al.* 1995; Zaman & Foss 1997; Smith & Mungal 1998). The slight asymmetry observed here is probably due to the influence of the non-symmetrical geometry of the traversing and probe supporting mechanisms used. Furthermore, the normalized cross-correlations between both y-halves for the two U- and V-components plotted in this figure, as well as for the W mean velocity field also measured in series #1 and #2, are 0.960, 0.945 and 0.955, respectively. As a consequence, all horizontal plane measurements reported in the remainder of the paper (series #3, #4 and #5) were obtained with the rake of probes spanning just slightly over one half of the flow in the lateral y-direction.

The three components of the velocity vector measured in series #2 and #3 at $X = 5$ are presented in figure 3(*a*). Mean V and W are plotted as vectors and streamlines, while the mean U velocity is plotted as isocontours. The isocontours of U shown in figure 3(*a*) exhibit at $Y = 0$ a maximum value at $Z = 6$ and a minimum value at $Z = 4$, which coincide with the values reported under similar conditions by Keffer & Baines (1963), Kamotani & Greber (1971), Fearn & Weston (1978) and Schetz (1980). The centre of the CVP is located at $Y = 1.6$ and $Z = 3.6$, in agreement with the results of Karagozian (1986) and Fearn & Weston (1978). Figures 3(*b*), 3(*c*) and 3(*d*) show, respectively, the r.m.s. values of the streamwise, spanwise and vertical components of the velocity. The whole picture suggests that at $X = 5$ the wake region spans from the upper edge of the boundary layer ($Z = 1.5$) up to the lower jet interface, between $Z = 3$ and 4, where the CVP is located and the r.m.s. of the three velocity components attain maximum values. The upper jet interface can be located beyond $Z = 6$ where the r.m.s. decays to the background value of the crossflow stream.

The velocity data in figure 3 indicate that the maximum r.m.s. values of the three velocity components are of the same order of magnitude ($1\,\mathrm{m\,s^{-1}}$) and roughly coincide with the magnitude of the mean V and W. This is the reason why $U_{nor} = 1\,\mathrm{m\,s^{-1}}$ was selected to normalize data. Since the mean velocities that characterize the CVP are of the same order of magnitude as the r.m.s. values (signal-to-noise ratio ≈ 1),

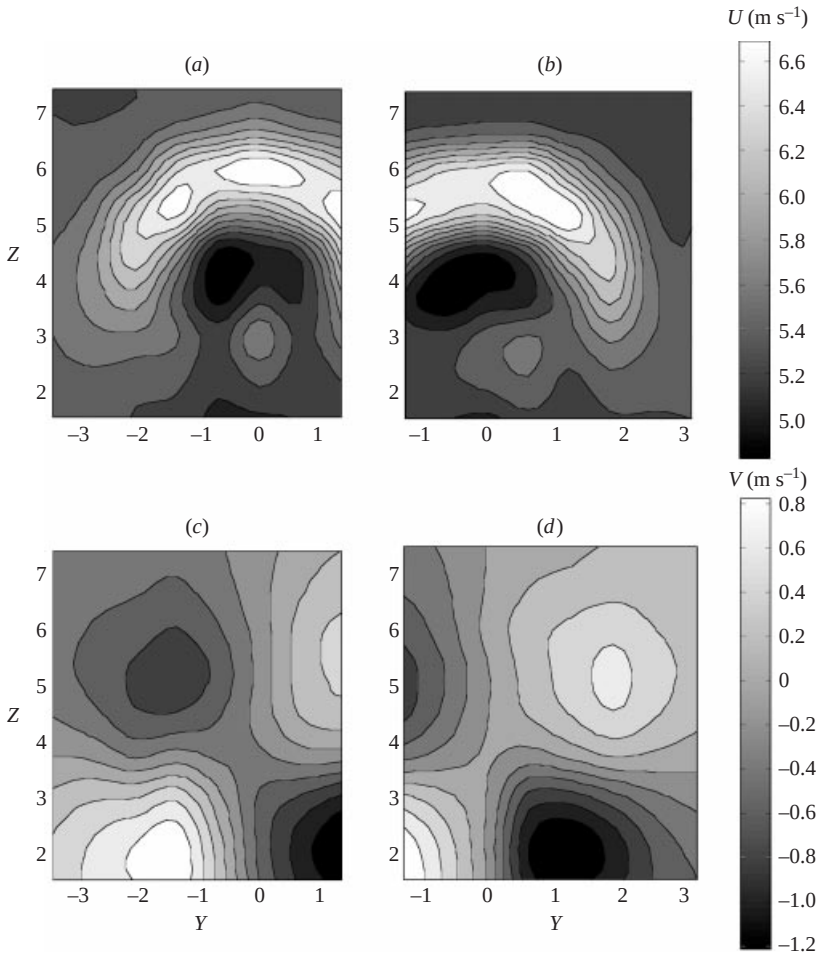

FIGURE 2. Symmetry of the mean velocity field measured in the (Y, Z)-plane of the jet at $X = 5$ (series #1 and #2). (*a*) Mean streamwise velocity $U(y, z)$ measured in the y-negative half of the jet; (*b*) mean streamwise velocity $U(y, z)$ measured in the y-positive half of the jet; (*c*) mean spanwise velocity $V(y, z)$ measured in the y-negative half of the jet; (*d*) mean spanwise velocity $V(y, z)$ measured in the y-positive half of the jet.

the instantaneous velocity field should have features with similar intensity to that of the CVP in the mean field and which are missed by the conventional time-averaging process. The PR analysis of the fluctuations should thus reveal the organization of the flow in addition to the CVP and which otherwise is buried by the time-averaging process.

3.2. *Two-dimensional coherent velocity maps*

The ensemble averages obtained by PR of the velocity data measured at several horizontal planes across the jet are presented in this section. To check that these ensemble averages are unbiased, i.e. that they do not depend on the initial template, various uncorrelated (orthogonal) initial templates and different threshold levels were tested. The results of this analysis are not included here, but they show that the ensemble averages presented are robust in the sense that they do not depend on the initial template. In addition it has to be mentioned that in the following plots we

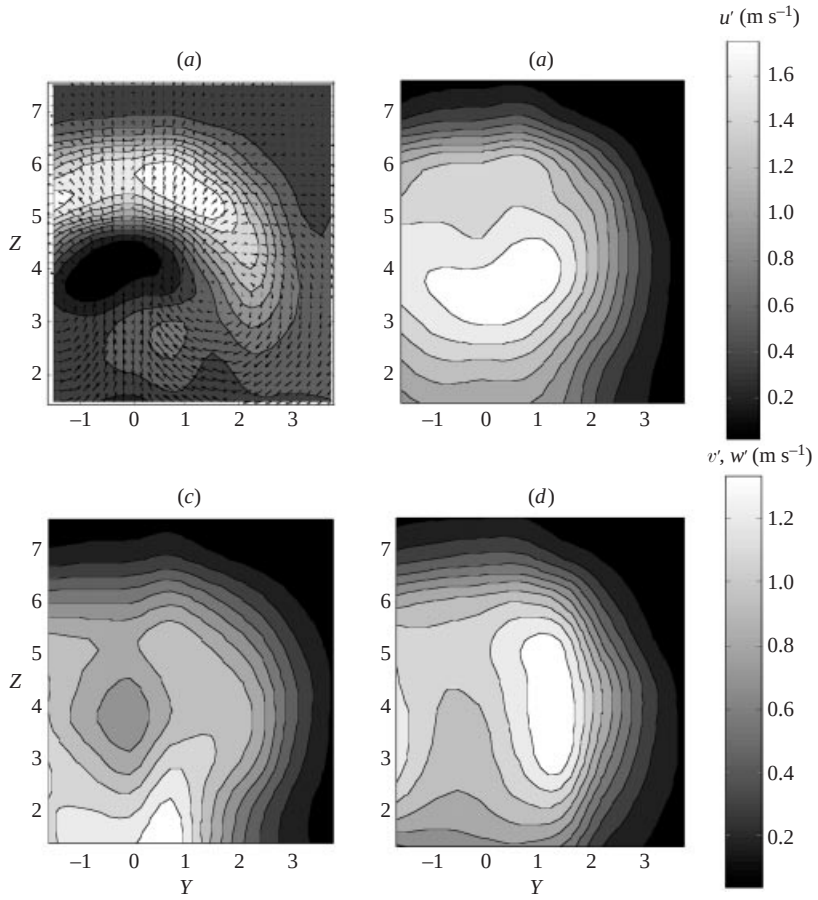

FIGURE 3. Mean and fluctuating velocity fields at $X = 5$. (*a*) Isocontours of the U velocity component and vector velocity map in the (Y, Z)-plane; (*b*) isocontours of U_{rms}; (*c*) isocontours of V_{rms}; (*d*) isocontours of W_{rms}.

include data of the three components of the velocity, while in the experiments the three components were measured but only two simultaneously, either (U, V) or (U, W). The procedure used to reconstruct the three-dimensional fields at each horizontal plane is as follows. The two files containing (U, V) or (U, W) were PR-analysed to identify the large-scale footprints in the U velocity signals. In the last iteration, the ensemble averages of the second velocity component, either V or W, simultaneously measured with U were also calculated from events at same location in the time records where coherent U-motions were identified. This process yields two ensemble averages, one with U and V, and another with U and W, that, after checking that the U coherent field is the same in both averages, are combined to produce a (U, V, W) ensemble average. The results are presented in figures 4 and 5 with the U- and V-components plotted as streamlines and the W-component plotted as grey isocontours, with the scale given below the last frame of each figure. In these and following figures the flow is from left to right with the jet flowing towards the reader.

Figure 4(*a–i*) shows equally z-spaced slices of the flow at $X = 5$, from $Z = 1.5$ to $Z = 7.5$. The jet centreplane is located at $y = 0$ and the time coordinate has been plotted as an x-coordinate through $\Delta x = -U_{conv}\Delta t$, with $x = 0$ placed arbitrarily but

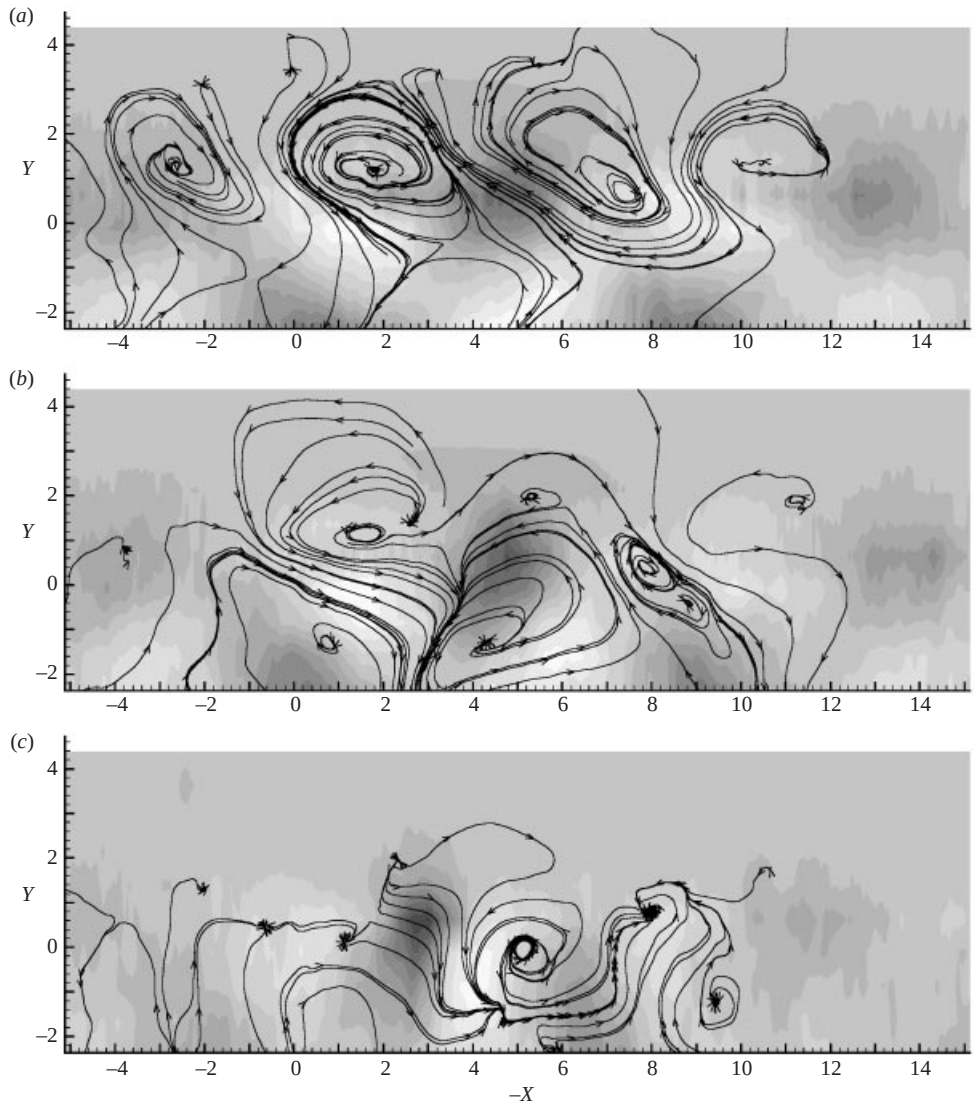

FIGURE 4 (*a–c*). For caption see page 130.

consistently at 25% of the x-span plotted. It has to be taken into account that all these results are presented as ensemble averages of velocity fluctuations, and no attempt has been made to convert them into 'camera' ensemble averages. This is so because the mean velocity field has not been added to the raw results and the convection velocity, $U_{conv} = U_{cf}$, has only been used to transform the time scale into a length scale. Even though the actual convection velocity of the vortices could change with the z-coordinate, mainly within the jet region, a constant convection has been used to plot the data in order to maintain the time span of measurements. This still results in a change of scale in the x-direction, with a small relative displacement between plotted z-planes, but not in a change in topology of the observed flow motions. It should also be noted that data measured at the different horizontal z-planes reported in figures 4, 5 and 6 could show some degree of asymmetry around $Y \approx 0$ because it

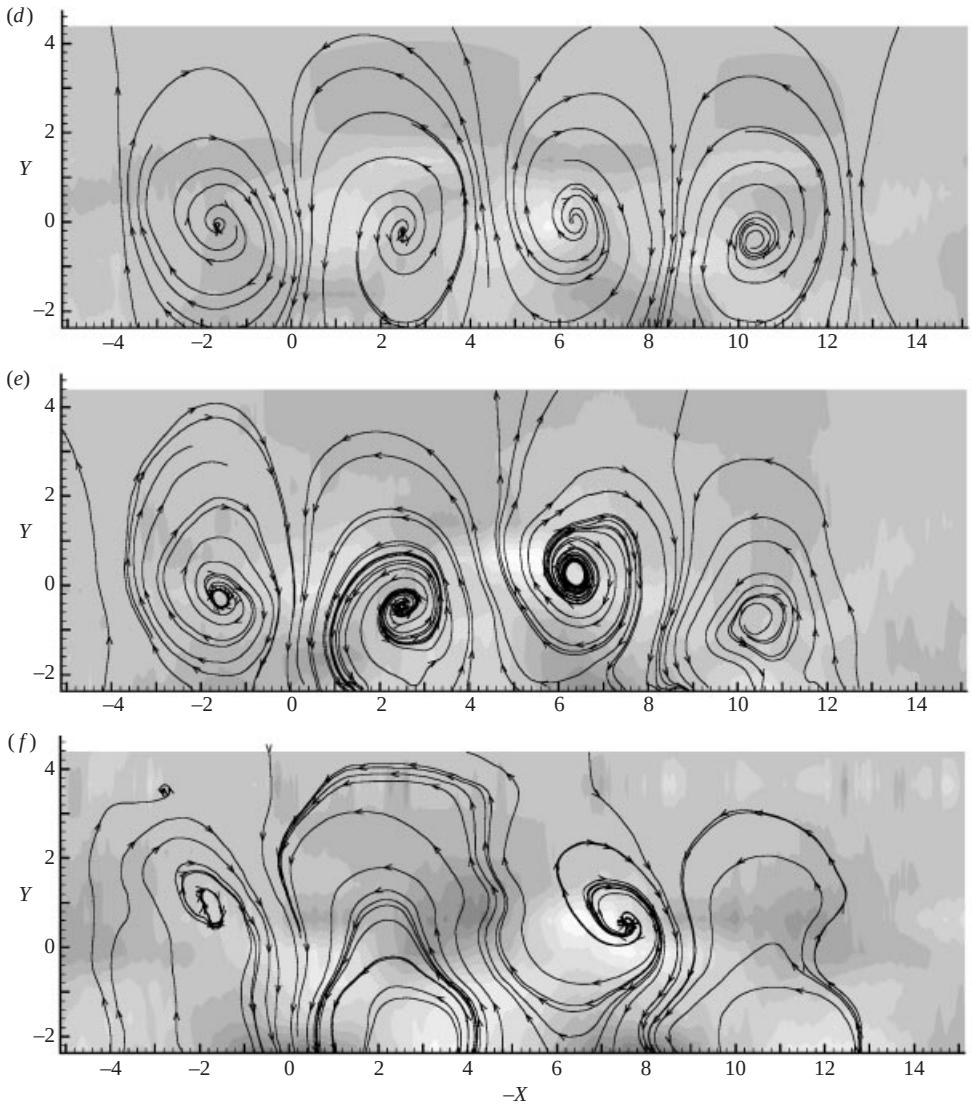

FIGURE 4 (*d–f*). For caption see page 130.

was only recorded for 30 s and the plots are the result of the PR analysis carried out over mostly one-sided data in the positive Y-direction.

Figure 4(*a*) a shows that close to the wall, at $Z = 1.5$, the flow is almost periodical and resembles the near wake behind a cylinder. The periodicity is a true characteristic of the flow because this feature was not in the initial template, which only contained two vortices centred at $X = 2.5$ and $X = 6.5$. The Strouhal number calculated from figure 4(*a*) is $St = 0.125$, which matches the values reported by other authors (see for example Fric 1990) and the spectral results for the U velocity, with a peak at $f = 30$ Hz ($St = 0.12$). Because the PR algorithm detects one by one all the events contributing to the ensemble average, it is possible to check that this periodicity is limited to isolated groups of vortices, which appear repeatedly in the flow, but that are separated by regions of less organized flow.

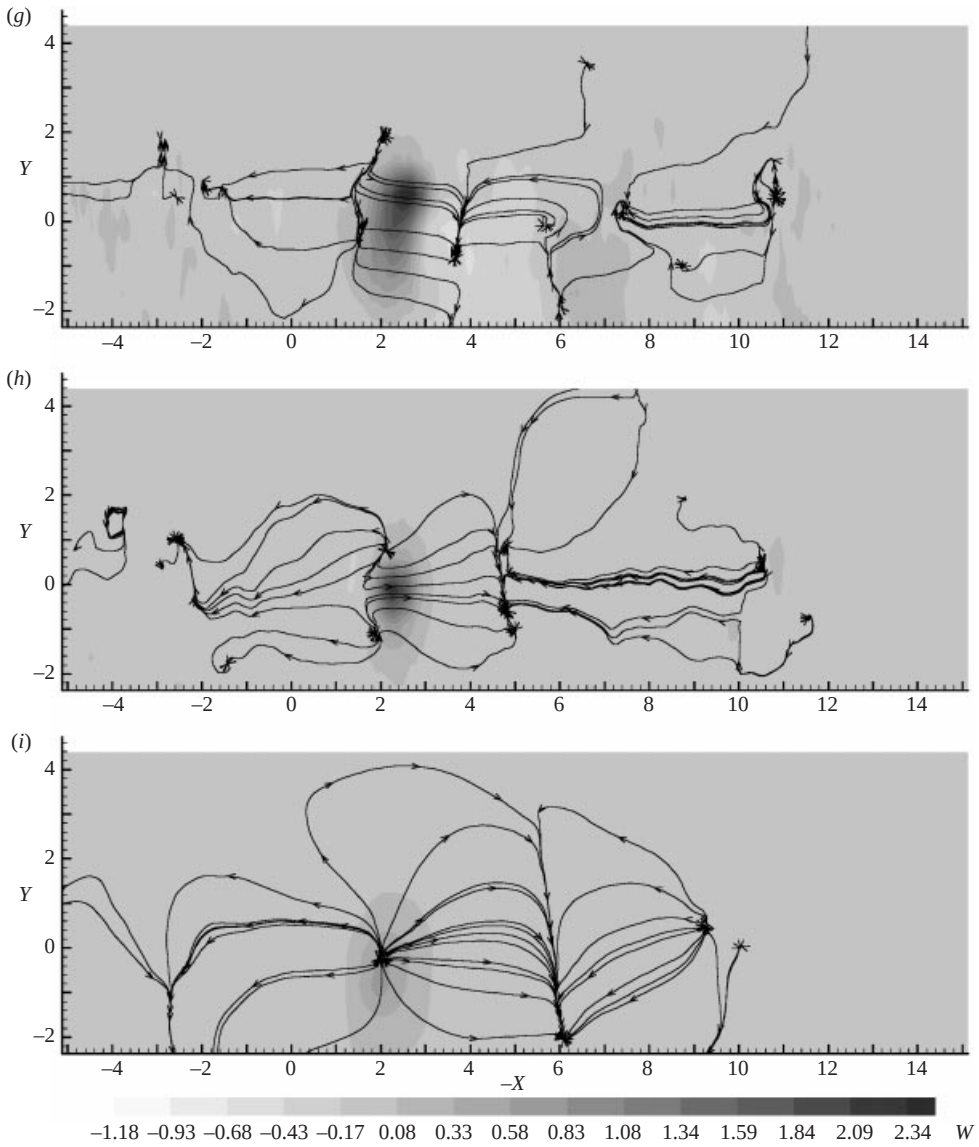

FIGURE 4. Horizontal slices showing the three components of the coherent velocity at $X = 5$. U- and V-components are plotted as streamlines and the W-component is plotted in grey levels. (*a*) $Z = 1.50$; (*b*) $Z = 2.25$; (*c*) $Z = 3.00$; (*d*) $Z = 3.75$; (*e*) $Z = 4.50$; (*f*) $Z = 5.25$; (*g*) $Z = 6.00$; (*h*) $Z = 6.75$; (*i*) $Z = 7.50$.

The fluctuating flow organization obtained at $Z = 2.25$ (figure 4*b*) is a transition to the pattern at $Z = 3$ (figure 4*c*) which shows that the cores of the Kármán-like vortices separate from the plane of symmetry of the jet ($Y = 0$) and initiate a branching of the initially centred upright vortices, which is also visible in the next z-plane. This branching was reported by Eiff & Keffer (1997) and is seen in their figure 10. Figure 4(*d*) corresponds to the patterns observed at $Z = 3.75$, where the CVP cores are located. This figure shows only one row of vortices aligned in the streamwise direction since the velocity field on the other side of the plane of symmetry

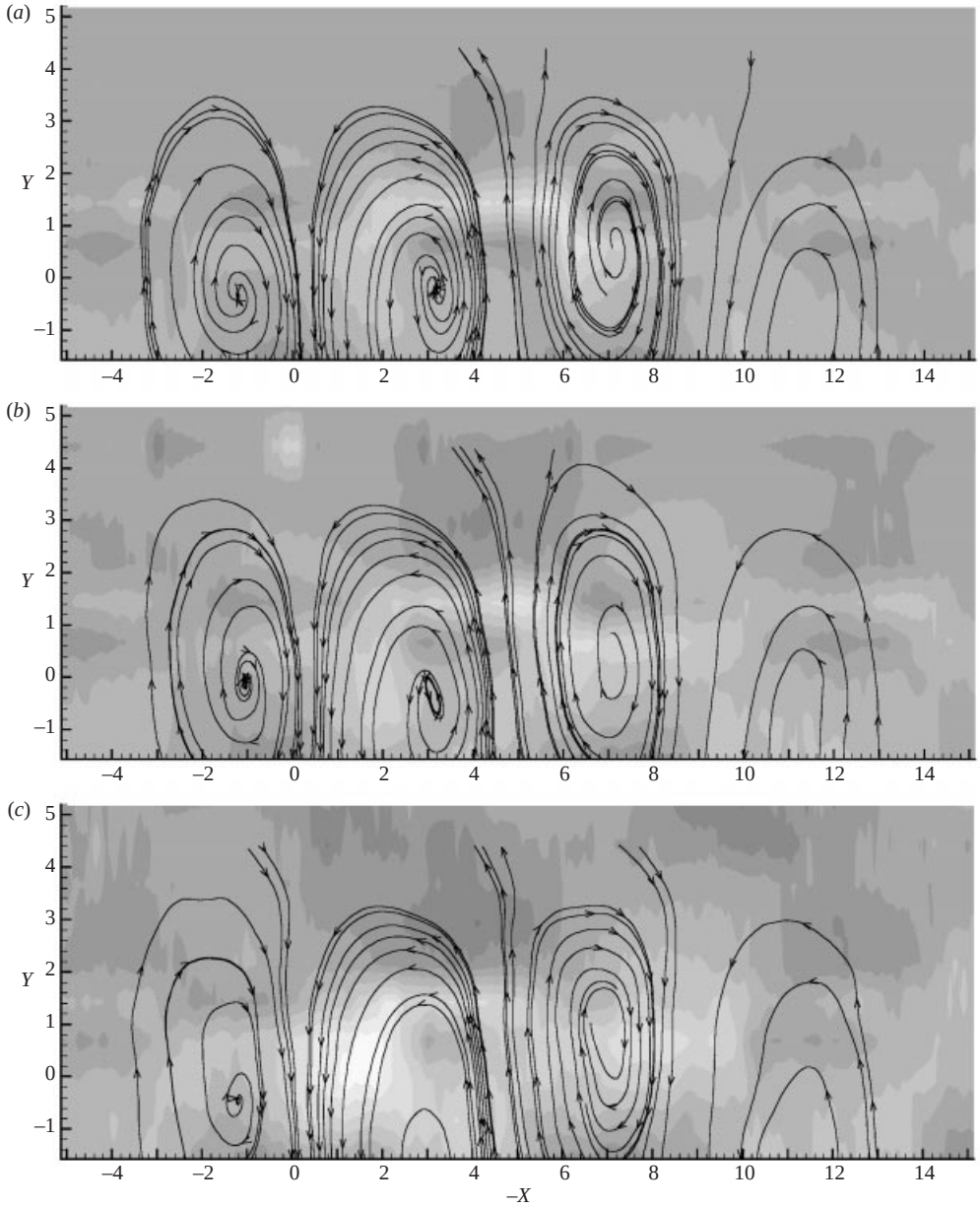

FIGURE 5 (*a–c*). For caption see page 134.

plane where the other row is located was not measured. The circulation of the CVP is located in a vertical plane (Y, Z), perpendicular to the plane of observation, and has mean V- and W-components. Since the patterns in figure 4(d) are obtained as ensemble averages of velocity fluctuations, the observed non-uniformity in the V-velocity (plotted as streamlines together with U) and in the W-velocity (plotted as isocontours) illustrates the modulation of the mean V and W velocity field of the CVP caused by the organized motions present at the lower jet interface. These motions seem to be the connection of the Kármán-like vortices to the CVP.

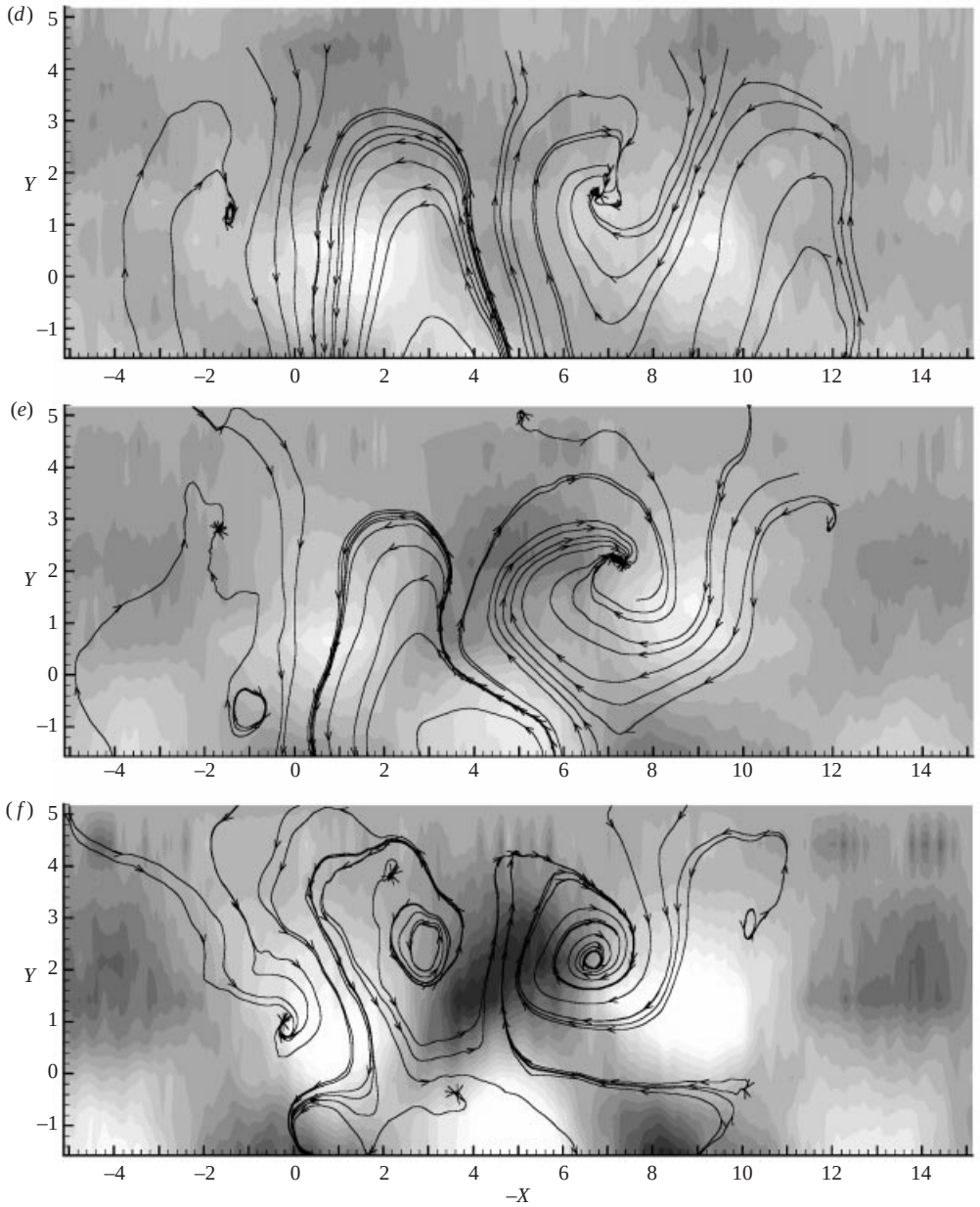

FIGURE 5 (*d–f*). For caption see page 134.

Figure 4(*e*) (at $Z = 4.5$) still bears some resemblance to figure 4(*d*), but the patterns displayed in figures 4(*f*) and 4(*g*) (at $Z = 5.25$ and 6, respectively) belong to the core of the jet, and are no longer dominated by the U- and V-components and the streamlines become less coherently significant. The indentations of the upper side of the jet begin to appear at $Z = 5.25$, where pockets of fluid moving in and out the plane of measurement are observed in figure 4(*f*) (isocontours of W alternating sign). Finally figures 4(*h*) and 4(*i*) correspond to the upper jet interface at $Z = 6.75$ and 7.5, respectively. The most striking feature of these two last sets of ensemble averages

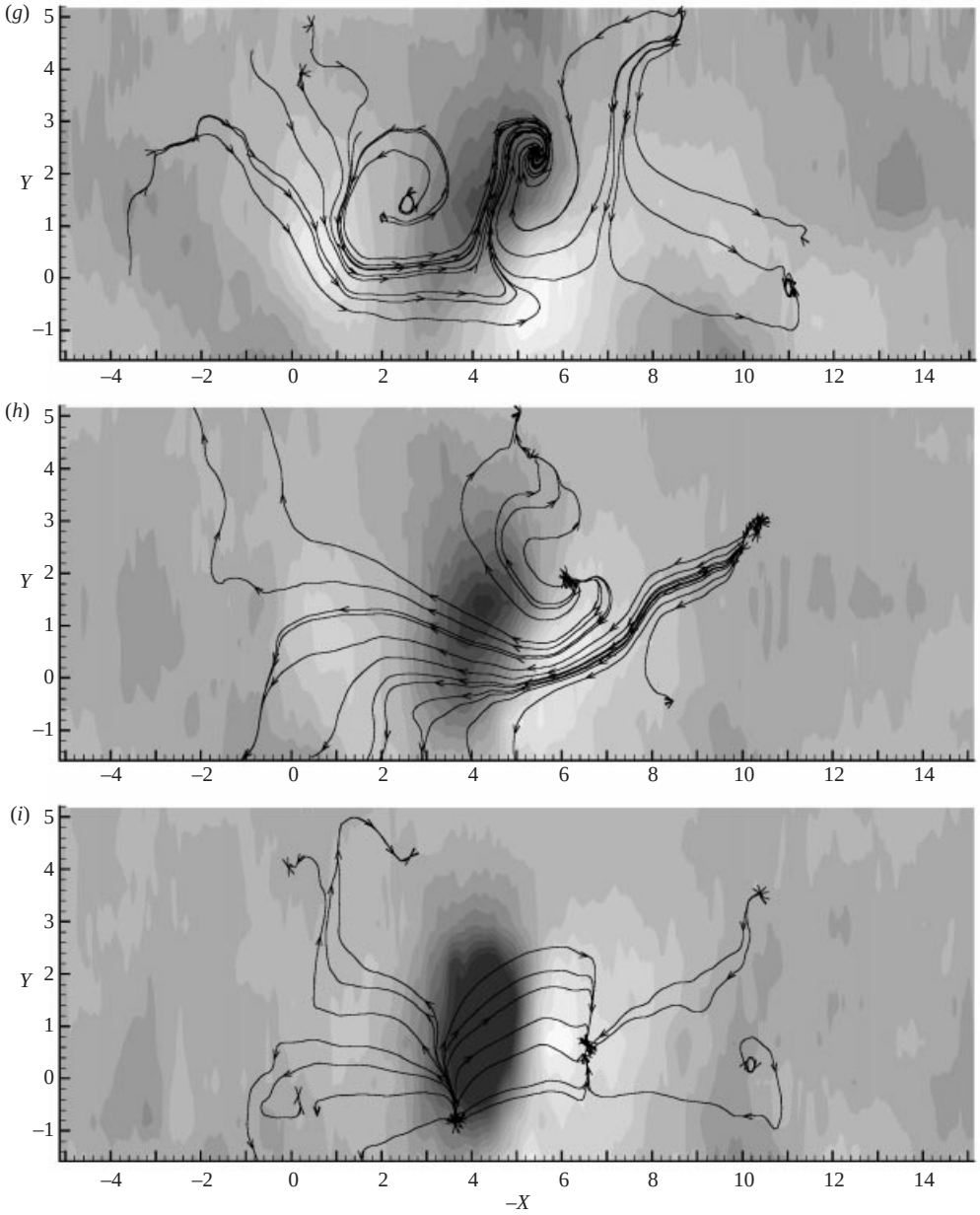

FIGURE 5 (*g–i*). For caption see page 134.

is the strong ejection of fluid observed at $-X = 2.5$, a feature that is supported by many flow visualizations.

Figure 5(*a–j*) shows equally z-spaced slices of the flow at $X = 15$, similarly to figure 4. In this case data were sampled in horizontal planes from $Z = 1.5$ to $Z = 8.25$, in steps $\Delta Z = 0.75$. It should be noted that at $X = 15$ the centre of the jet has moved to a higher z-coordinate ($Z = 7$), and the lower jet interface is now approximately located between $Z = 4$ and $Z = 5$, and the upper jet interface beyond $Z = 8$. The patterns observed at $X = 15$ display features parallel to those observed

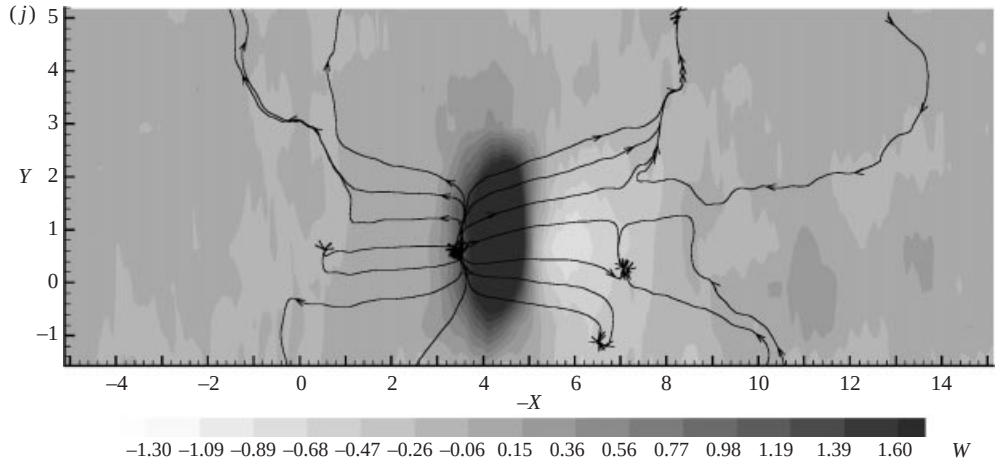

FIGURE 5. Horizontal slices showing the three components of the coherent velocity at $X = 15$. U- and V-components are plotted as streamlines and the W-component is plotted in grey levels. (*a*) $Z = 1.50$; (*b*) $Z = 2.25$; (*c*) $Z = 3.00$; (*d*) $Z = 3.75$; (*e*) $Z = 4.50$; (*f*) $Z = 5.25$; (*g*) $Z = 6.00$; (*h*) $Z = 6.75$; (*i*) $Z = 7.50$; (*j*) $Z = 8.25$.

at $X = 5$. The patterns in figure 5(*a–c*) ($Z = 1.5$, 2.25 and 3, respectively) occur in the wake region, while those in figure 5(*d–f*) ($Z = 3.75$, 4.5 and 5.25, respectively) are located in the zone dominated by the CVP, and show again the modulation of the instantaneous field. Figures 5(*g*) and 5(*h*) ($Z = 6$ and 6.75, respectively) correspond to the centre of the jet. Circulation in the plane of measurement weakens, and bulges of fluid moving in and out of this plane show again the indentation of the jet. Finally, figures 5(*i*) and 5(*j*) ($Z = 7.5$ and 8.25, respectively) show that a strong outward ejection of fluid from the jet to the cross-flow stream occurs across the upper jet interface.

The results depicted in figures 4 and 5 indicate that there is a clear separation of the different flow regions in terms of the different patterns observed as z is increased from the boundary layer up to the upper jet boundary. The strong features displayed in the (U, V) maps in the horizontal planes nearer to the wall and in the W isocontours in the upper region are a clear indication of the robust organization present in a jet in crossflow. It is thus interesting to display the ensemble averages reported in figures 4 and 5 as they would be seen by an observer moving at a constant convection velocity $U_{conv} = U_{cf}$. Only the results obtained at $X = 5$ are presented in this frame of reference because the organized motions at this location are well-defined and not significantly different from those at $X = 15$, as shown in figures 4 and 5 for the instantaneous field. Figure 6 shows the same ensemble averages for the different z-planes as presented in figure 4, after adding the mean velocity field, $\boldsymbol{V}_m = [U_m(x, y, z), V_m(x, y, z), W_m(x, y, z)]$ (see figure 2), and subtracting the constant convection velocity, U_{cf}. Note that, for example, $U_m(y)$ for any z-plane across the jet is usually larger farther from the centreline $Y = 0$ and, thus, circulations in figure 6 are modified with respect to those in figure 4, i.e. depending on their sign some circulations observed in figure 4 appear reinforced, but distorted and tilted, in figure 6, while others are converted into saddles. Furthermore, even though a constant convection velocity $U_{conv} = U_{cf}$ is not the best choice to visualize circulations in each z-plane, it is the only consistent way to relate them to the vorticity field without adding the artificial vorticity that would result from the alternative choice $U_{conv} = U_{conv}(z)$.

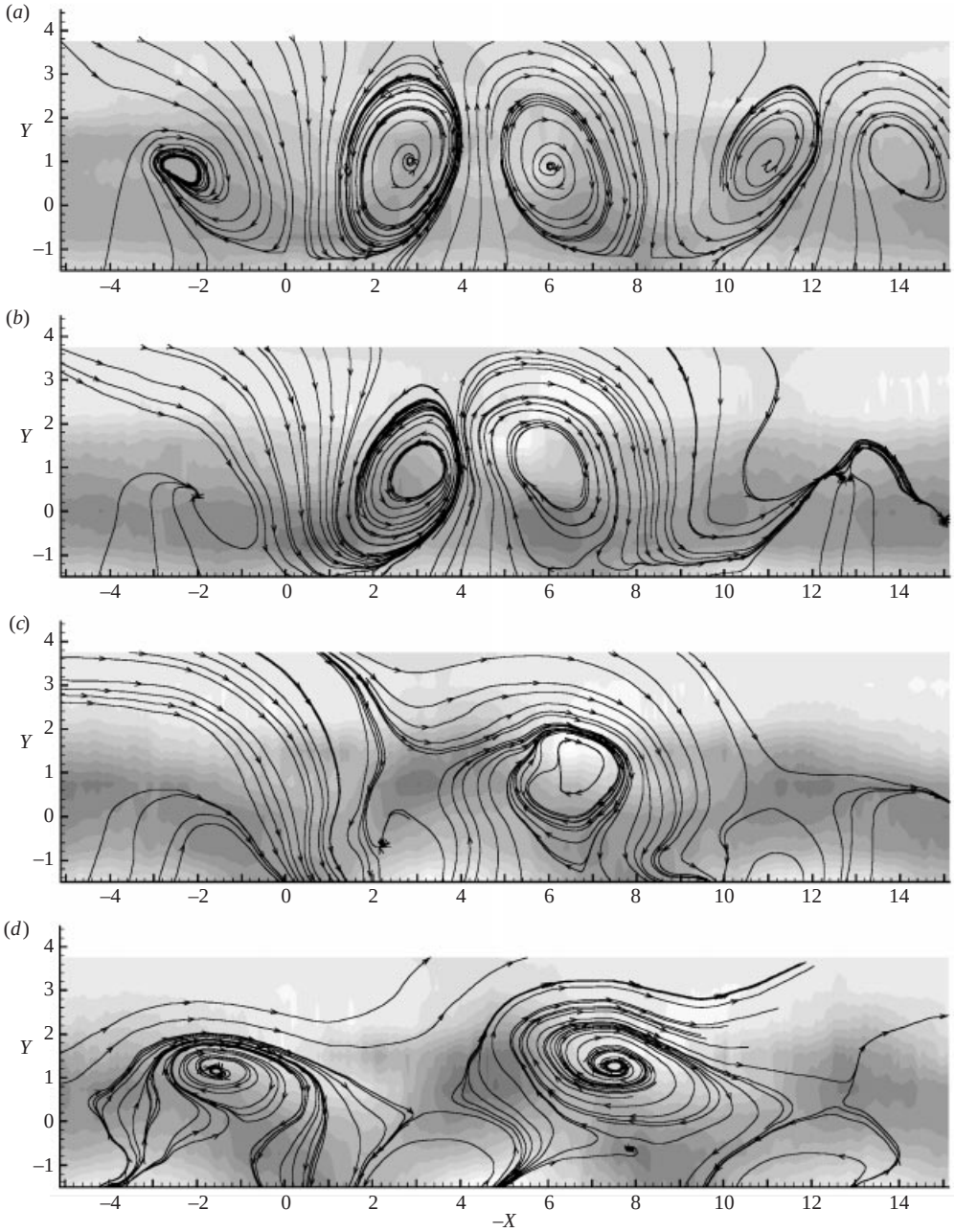

FIGURE 6 (*a–d*). For caption see page 137.

Figure 6 depicts horizontal slices of the modulated CVP because they are the feature of the mean velocity field. Close to the wall at $Z = 1.5$ (figure 6*a*) the addition of the mean velocity field does not change dramatically the Kármán-like vortices. The reason is that the velocity defect in the pseudo-wake is very weak compared to that in the wake of a cylinder. However, some changes are observed; the most important is that now the pseudo-Kármán vortices appear alternately tilted upstream or downstream,

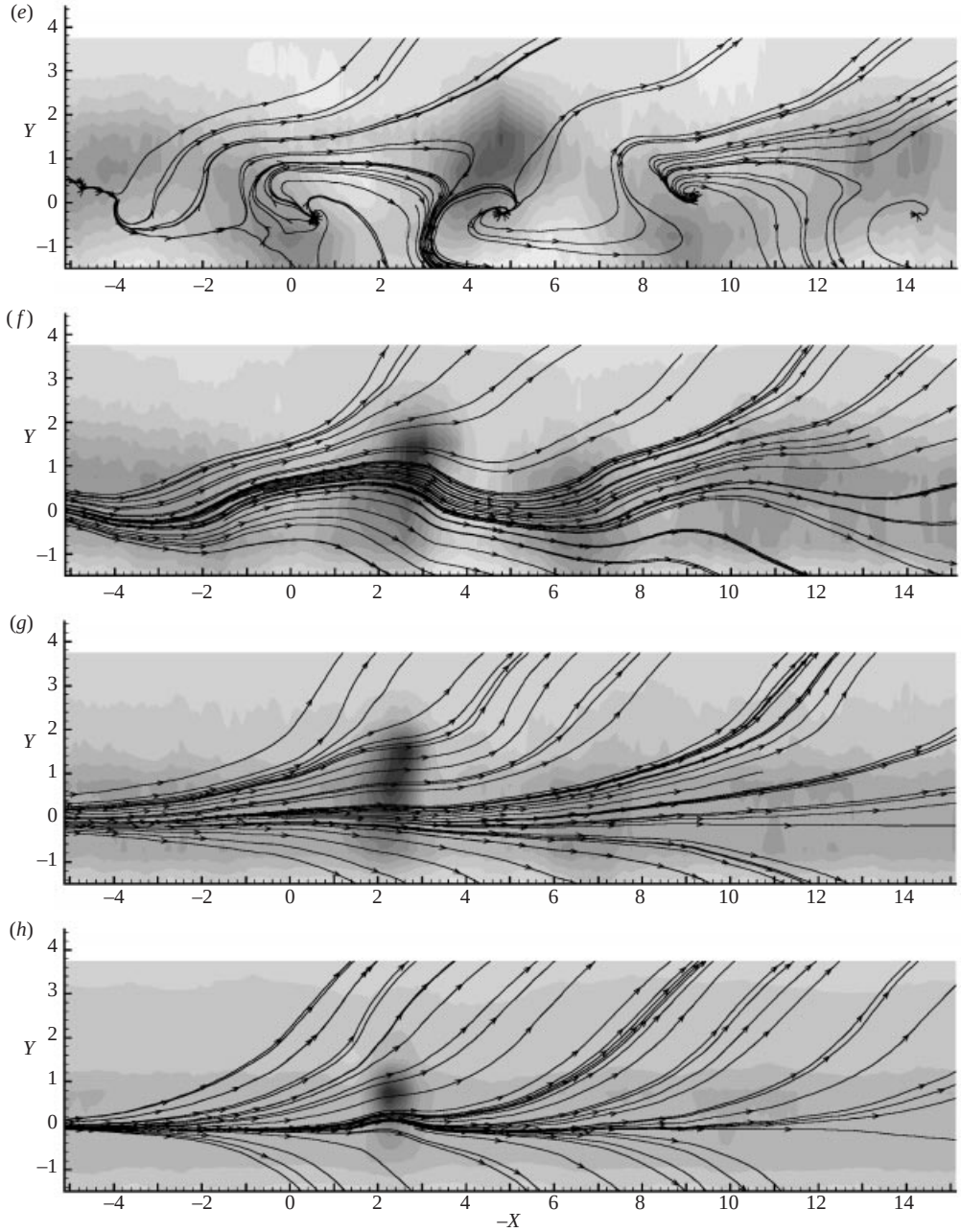

FIGURE 6 (*e–h*). For caption see page 137.

depending on their sense of rotation. The organization at $Z = 2.25$ (figure 6*b*) is still a transition from that in figure 6(*a*) towards the saddle point distribution that appears in figure 6(*c*) at $Z = 3.0$, which would appear as a circulation if a higher convection velocity had been subtracted from the mean field $V_m(y)$. This distribution should be analysed in conjunction with figures 4(*b*) and 4(*c*). Figure 4(*c*) shows that the cores of the Kármán-like vortices separate from the plane of symmetry of the

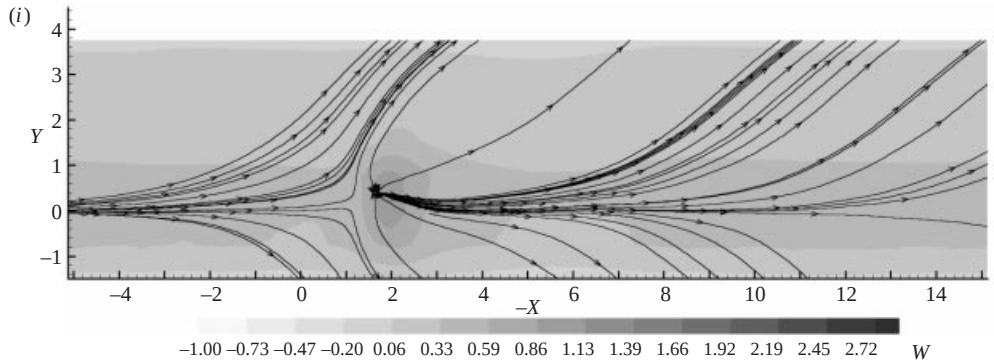

FIGURE 6. Horizontal slices showing the three components of the total velocity at $X = 5$ as seen by an observer moving at U_{cf}. The results correspond to those presented in figure 4 as raw ensemble averages.

jet, compared to their position in figure 4(*b*), as the vertical distance from the wall increases. In addition, the vortices moving towards more negative lateral y-positions seem to generate another vortex at $-X = 2.5$ and $Y = 1$, with the same sense of rotation, filling the void left by this shift. However, when this is analysed in figure 6(*c*) including the mean vorticity, it is clear that this 'new vortex' is not a focus but a saddle, centred at $-X = 2.5$ and $Y = 1$. In addition, the vortex at $-X = 6.5$ and $Y = 1$ is reinforced.

The modulation of the CVP is very clear at $Z = 3.75$ where the CVP cores are located (Figure 6*d*). First, the W-component of the velocity (remember that the CVP have V and W) is a modulated band that, from left to right, attains positive values near the centreplane (upward flow) and negative values at the edge (downward flow). But the V-component is only positive at $-X = 3$ or $-X = 6$, and negative at $-X = 1$ and $-X = 10$. In addition, the circulation in the plane of measurement is very clear, displaying how the Kármán-like vortices of the wake 'connect' to the CVP. The similarity between figures 6(*e*) and 6(*d*) is much weaker than the similarity between figures 4(*e*) and 4(*d*). At a vertical position $Z = 4.5$ (figure 6*e*) the rake is located above the centre of the CVP and approaching the core of the jet. The structures at $Z = 5.25$, 6 and 6.75 depicted respectively in figures 6(*f*)–6(*h*) are dominated by the excess of U velocity in the jet, because the selected convection velocity U_{cf} is smaller than the U velocity at the centre of the jet. An important feature in these three plots is still the ejection of fluid between $-X = 2$ and $-X = 3$. Finally, at the upper edge of the jet ($Z = 7.5$ in figure 6*i*) the strong vertical ejection of fluid that occurs at $-X = 2$ becomes a saddle-node.

Figure 7 shows the photographs of the instantaneous flow obtained with PLIF at the three (y, x)-planes $Z = 3$, 5 and 7, and recorded with a ground-fixed camera. The wake flow characteristics that are evident near the centreplane ($y = 0$) at $Z = 3.0$ in figure 7(*a*) are consistent with the corresponding velocity slices given in figures 4(*c*) and 5(*c*), and with figure 6(*c*) if the effect of the convection velocity is taken into account in the visualization. The same is true but more smeared when figures 6(*e*) and 7(*b*) ($Z = 4.5$ and 5.0) are compared. This pseudo-wake flow structure visualized in figures 7(*a*) and 7(*b*) near the centreplane, which is dominated by the sequence saddle–focus–saddle points, as clearly observed in figure 6(*c*) and with still a remnant in figure 6(*e*), is the same as the dominant structure educed in the intermediate wake behind a cylinder by Vernet, Kopp & Giralt (2000). To understand the flow patterns

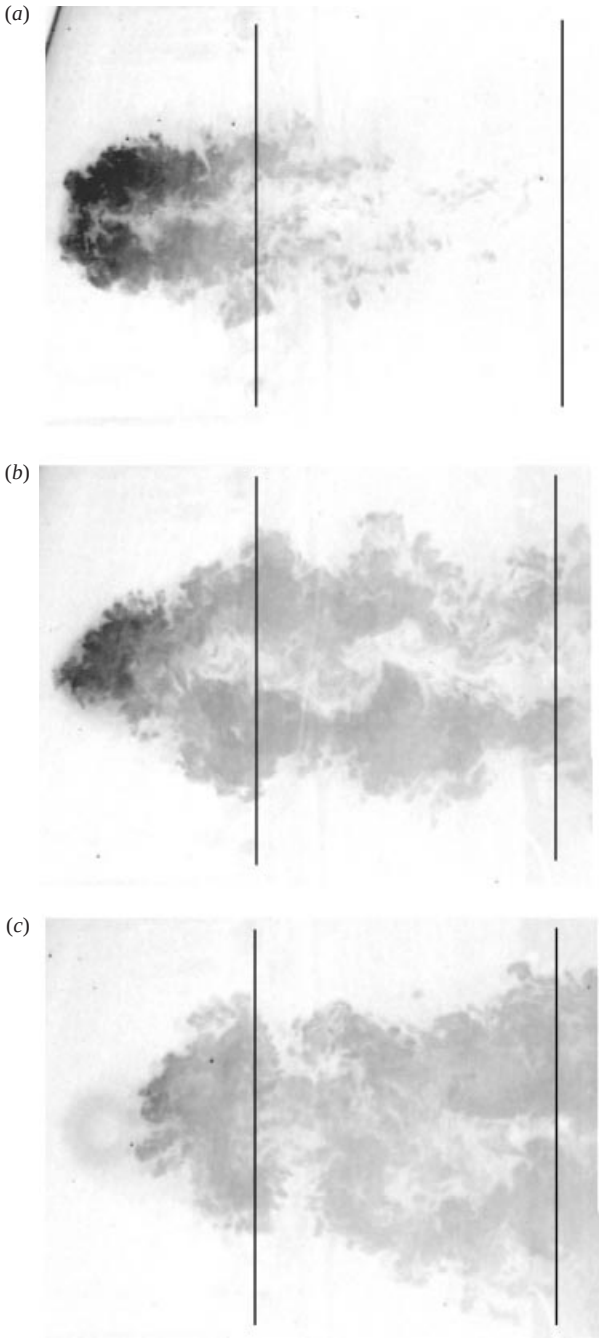

FIGURE 7. Instantaneous visualizations obtained by PLIF at horizontal planes located at (*a*) $Z = 3$; (*b*) $Z = 5$; (*c*) $Z = 7$. Reference lines at $X = 5$ and 15 are also included.

measured and visualized at the upper edge of the jet ($Z = 7$), shown respectively in figures 6(*h*) and 6(*i*), and 7(*c*), it is convenient to examine in more detail this upper interface of the jet.

The visualization of the jet centre vertical plane (z, x-plane at $y = 0$) in figure 8

FIGURE 8. Instantaneous visualization obtained by PLIF at the vertical centreplane to illustrate the roll-up process in the upstream jet interface. The arrows indicate the shear layer vortices and how the distance between them is roughly doubled in successive steps.

suggests that the upper interface indentations (ejections of fluid in figures 4*h*, *i*, 5*h*, *i* and 6*c*) are the results of the pairing and doubling-period process undergone by the forward or upstream face of the jet in the early stages of development. The leeward side rapidly becomes turbulent but the lateral sides also form a skewed mixing layer and the question arises whether some trace of the pairing process remains in the far field. Unfortunately, the present hot-wire data have insufficient spatial resolution to answer this question. Nevertheless, the numerical calculations by Yuan *et al.* (1999) with LES (see figures 13 and 14 of their paper) suggest that this is a real possibility.

3.3. *Three-dimensional coherent field*

The data used to obtain the ensemble averages for the three velocity components at the consecutive Z-planes plotted in figures 4, 5 and 6 were measured in different experiments. As explained previously, the analysis of these data started with the plane closest to the wall, where different initial templates and threshold levels were checked. Subsequently, it was applied to the following consecutive (y, x)-planes using as initial template for the PR analysis the final ensemble average obtained in the previous plane. This sequence of analysis implicitly assumes that the ensemble averages obtained from different experiments are actually slices through the same three-dimensional coherent structure since the ΔZ intervals between planes are small. However, a complete three-dimensional reconstruction of the coherent structure requires a thorough check of the above hypothesis since even though the flow is stationary and ergodic the experiments are certainly different.

The first check was to compare the fraction of the recorded data that contributed to the ensemble averages in different Z-planes. The fractions attained were always in the range 20%–25%, increasing to 30% in the upper slices of the flow. Therefore, the flow

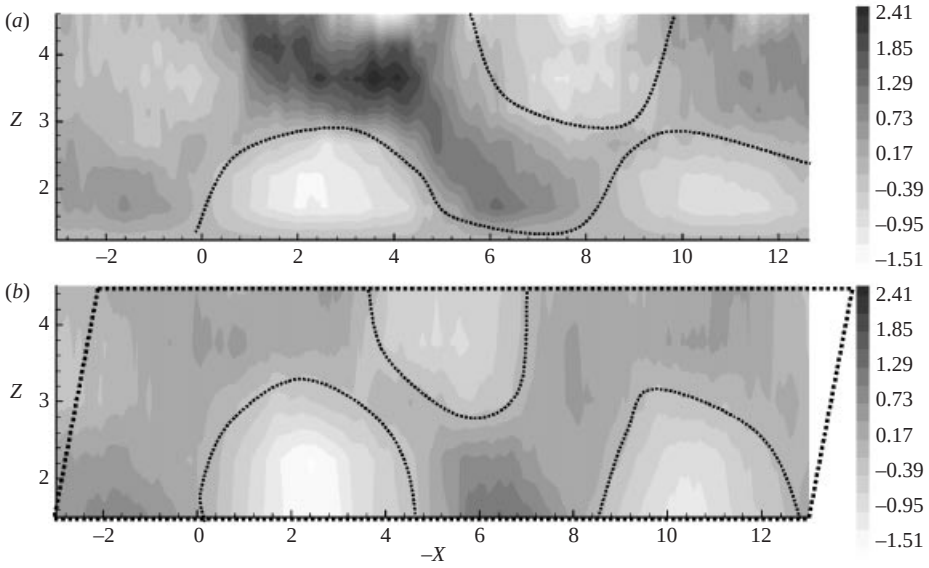

FIGURE 9. Modulus of the velocity $(U^2 + W^2)^{1/2}$ at $Y = 1$. (*a*) Results obtained from direct vertical plane measurements (series #6 in table 1); (*b*) reconstructed vertical plane results from the assembled horizontal plane measurements.

organization plotted in figures 4, 5 and 6 represents about $\frac{1}{4}$ of the whole flow. The process of assembling the coherent patterns from different experiments to reconstruct the full three-dimensional topology of the organized motion consists in appropriately aligning the x-coordinate of the different individual slices of the flow. To evaluate the reliability of the alignment process, a synthetic vertical slice through the large-scale motion obtained from the three-dimensional assembled data is compared in figure 9 with a directly measured vertical slice of the flow in the experiments of series #6, where the probes spanned the z-direction. The reconstructed organized motion in the vertical plane $Y = 1$, depicted in figure 9(*a*) in terms of the modulus of the velocity $(U^2 + W^2)^{1/2}$, compares well qualitatively with the pattern in figure 9(*b*), which was directly educed from measured vertical data. The most noteworthy difference observed is in the vertical alignment of the x-coordinate of the reconstructed horizontal slices in figure 9(*a*), which should be slightly slanted to the right (as indicated by the dotted lines in this figure) to improve the matching between both vertical patterns.

The three components of the large-scale coherent vorticity, Ω_x, Ω_y and Ω_z, computed at $X = 5$ from the three-component fluctuating velocity data assembled from the horizontal planes in figure 4, are depicted respectively in figures 10(*a*)–10(*c*). The CVP is not visible in figure 10(*a*), where Ω_x is plotted, because this coherent vorticity has been obtained from velocity fluctuations that do not contain the information of the mean velocity profile. However, it is easy to work out what the appearance of the CVP in figure 10(*a*) would be: two vortex tubes with vorticity of opposite sign along the x-coordinate, centred at $Y = \pm 1.6$ and $Z = 3.6$ and overlapping the Ω_x of the coherent motions, which is of the same order of magnitude. The highest Ω_x isolevel plotted in figure 10(*a*) is ± 0.33 because isosurfaces with higher vorticity are located within those isosurfaces shown. The coherent Ω_x is in the range ± 3 compared to the $\Omega_x = \pm 2$ attained approximately by the CVP. Therefore, the instantaneous CVP are vortex tubes alternately modulated in intensity by the coherent motions; when the

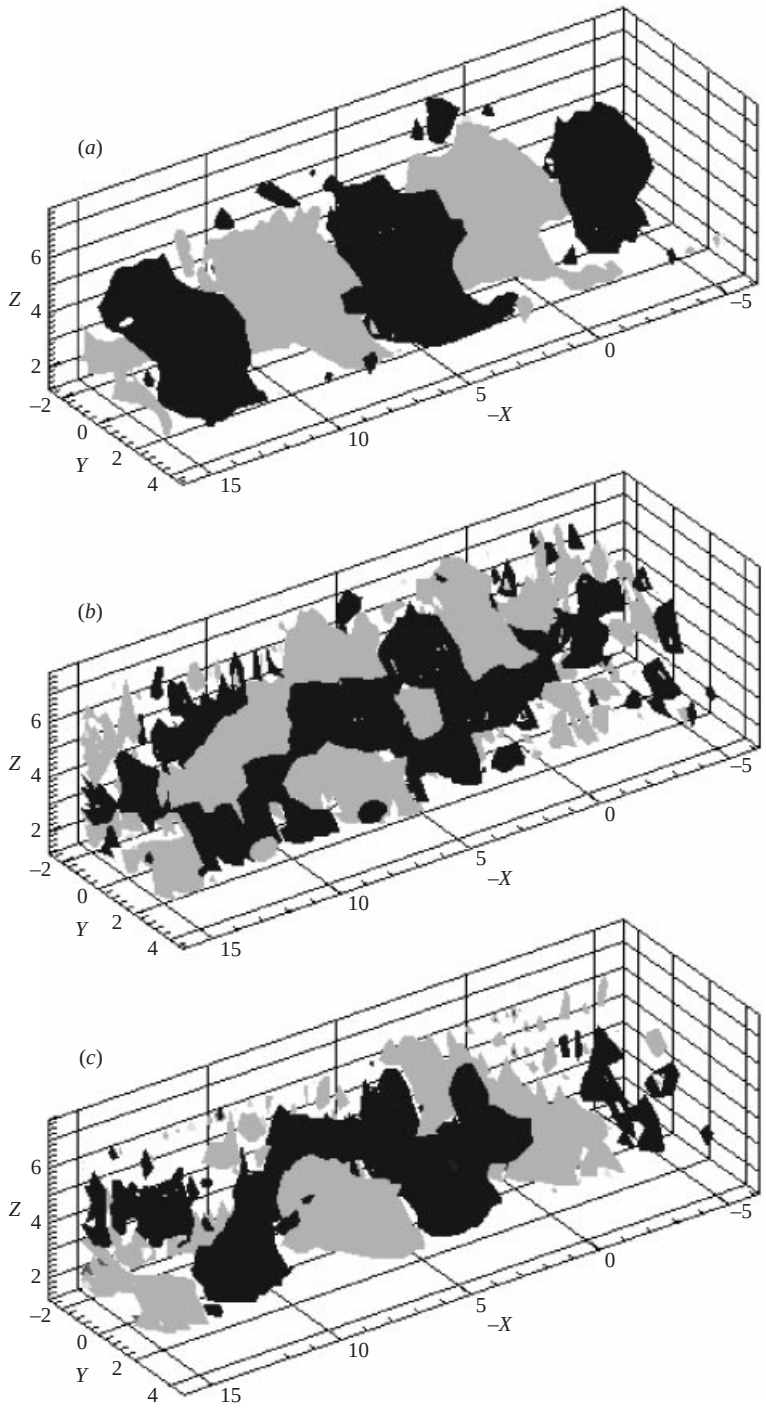

FIGURE 10. Three-dimensional coherent vorticity field at $X = 5$. (*a*) Isosurfaces of $\Omega_x = 0.33$ and -0.33; (*b*) isosurfaces of $\Omega_y = 0.33$ and -0.33; (*c*) isosurfaces $\Omega_z = 0.66$ and -0.66. Positive values correspond to darker greys and negative levels to lighter ones. In this figure the flow is from right to left to depict a clearer picture of the coherent vorticity.

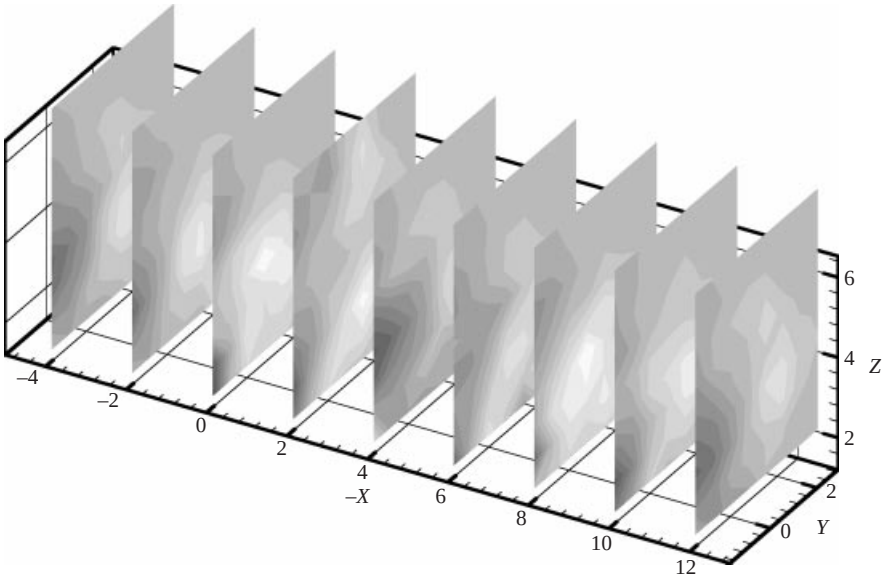

FIGURE 11. Sequence of vertical slices through the total Ω_x vorticity field of the coherent CVP for $-1.5 \leqslant Y \leqslant 3.75$ at $X = 5$. The CVP located at the positive-Y side is identified with the lighter grey level.

$+\Omega_x$ vortex is stronger the $-\Omega_x$ vortex is weaker, and vice versa. Obviously, when this flow organization is time-averaged, this modulation and coupling disappears, and the two vortices appear symmetrical. This modulated organization, previously observed in the flow visualizations of Smith *et al.* (1993) and Smith & Mungal (1998), is quantitatively documented in figure 11 where several vertical slices through the total Ω_x vorticity field, i.e. the vorticity of the coherent field already displayed in figure 10(*a*) plus the vorticity of the mean field, are presented. The data in figure 11 span from $Y = -1.5$ to 3.75 and, therefore, display mainly the lateral oscillations of Ω_x corresponding to the vortex located at the positive-Y side of the CVP (identified with the lighter grey level). At both $-X = 8$ and $-X = 0$ the core of this vortex is positioned nearest to the centreplane, which corresponds to a wavelength that matches the Strouhal number $St = 0.12$ measured in the wake region. It is difficult to see in figure 10(*b*) any organization in the ± 0.33 isocontours of the coherent Ω_y vorticity alone, but the ± 0.66 isocontours of Ω_z in figure 10(*c*) show a spatial distribution which resembles that of Ω_x. The main difference is that the lobes of Ω_x vorticity occur at higher z positions than the Ω_z lobes, which attain maximum values of $\Omega_z = \pm 9$ (three times higher than Ω_x) in the wake. The same sort of plots have been obtained at $X = 15$ but they are not presented here for the sake of brevity. The peak values of the three components of the coherent vorticity are lower at $X = 15$ than at $X = 5$, but the three-dimensional organization of the vorticity is similar.

To better understand the role of the large-scale structures present in the jet in crossflow it is convenient to visualize the three-dimensional organization of the vorticity in the flow. This is done by plotting simultaneously the three components of vorticity as vortex lines. Again, like in figures 10 and 11 there are two choices: to plot the coherent vorticity or the total vorticity field. The latter is presented in figure 12, which shows the vortex lines (plotted with a finite thickness) of the total vorticity field measured at $X = 5$. Integration of several trajectories through the vorticity field,

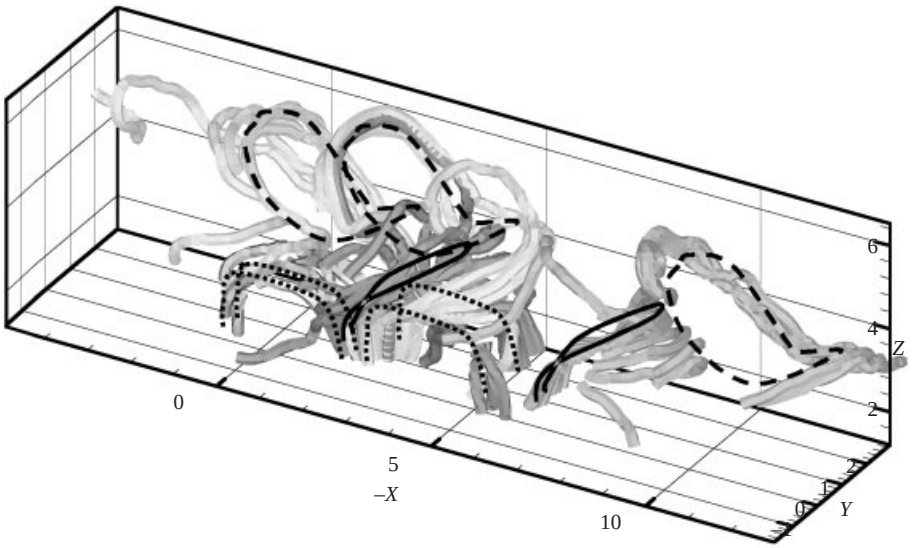

FIGURE 12. Total vorticity field at $X = 5$, displayed with vortex lines of finite thickness. Trajectories were integrated both forward and backward in time up to the edges of the domain.

starting at arbitrary points, in both forward and backward directions, produced the different plots in this figure. Although the lines differ in some details, they share some common features. To help the discussion of this figure, the vortex lines with a similar behaviour have been plotted using four different grey levels. The first feature that we can observe in figure 12 is that most of the vortex lines start or end in the lowest horizontal plane ($Z = 1.5$), on their way to connect with the boundary layer. Some of them are 'handle-type' vortex lines, arising from the boundary layer with vorticity Ω_z, having increasing Ω_x values away from the wall while bending horizontally, and returning to the boundary layer with $-\Omega_z$. These handle-type vortex lines appear at about $-X = 0$ and can be interpreted as connections between the Kármán-like vortices in the wake.

A second kind of vortical structure observed in figure 12 is the 'horseshoe', with its legs lying on the boundary layer. They are folded in the downstream direction, although other vortex lines are folded upstream in what appear to be 'folded vortex rings'. The horseshoes can be interpreted as vortex lines lying initially at the top of the boundary layer with vorticity Ω_y, that have been lifted by the jet, while the folded vortex rings have their origin in the initial azimuthal vorticity of the jet that have been folded by the interaction with the crossflow stream. Several authors have hypothesized about these structures. Eiff & Keffer (1997) plotted a vortex skeleton that contained some sort of connected horseshoes; however the flow that they studied was the jet in crossflow issuing from a stack. Andreopoulos (1985) and Kelso *et al.* (1996) conjectured the occurrence of folded vortex rings from visualization experiments. Sykes *et al.* (1986) found them in the results of a numerical simulation of the flow. The so-called handle-type structures are better visualized if the vorticity generated by the mean velocity field is removed, and only coherent vorticity is used to plot the vortex lines. The result of this operation is shown in figure 13, where the vortex lines obtained from only the coherent vorticity field at $X = 15$ are plotted. The isocontours of Ω_x at the horizontal plane $Z = 4$ approximately located at the lower jet interface are also included.

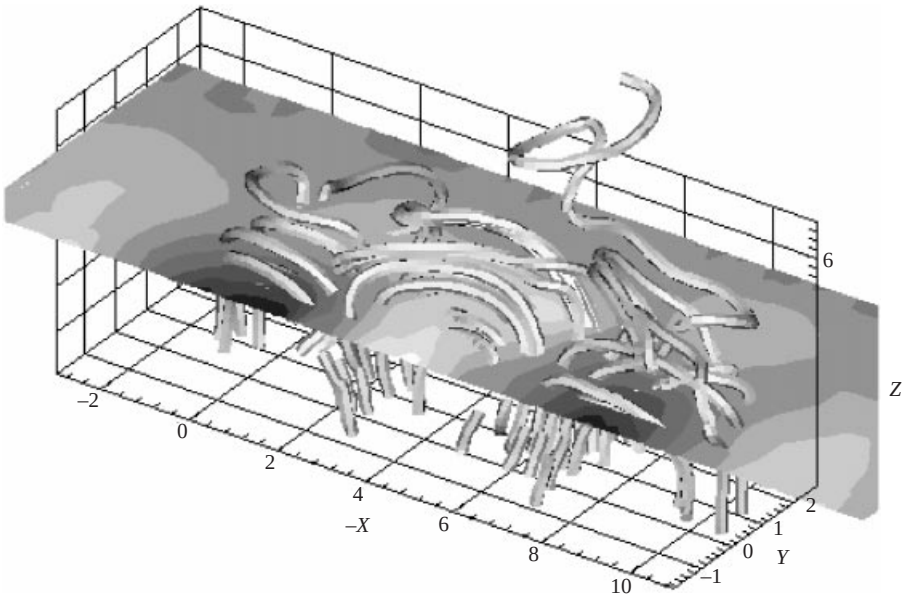

FIGURE 13. Total coherent vorticity field at $X = 15$, displayed with vortex lines of finite thickness, and isocontours of coherent vorticity Ω_x at $Z = 4$. The appearance of 'handle-type' structures at $X = 5$ is very similar but with shorter handles.

Figure 14 presents the streamlines obtained at $X = 5$ when several particles are released into the total velocity field to further clarify the vorticity field depicted in figure 12. These streamlines are calculated by integrating the trajectories of the particles in both forward and backward directions, and they are observed from a frame of reference moving at $U_{con} = U_{cf}$. Figure 14 also includes the isocontours of V at $Z = 1.5$. The results in this figure have to be interpreted with caution because the particles were released over a frozen velocity field within the unsteady flow sequence and, therefore, the plot is of instantaneous streamlines. Despite this limitation the streamlines reveal the presence of the CVP and of the Kármán-like vortices ascending from the boundary layer and connecting to the CVP in the y-positive half of the jet.

4. Concluding remarks

The structural characteristics of a turbulent jet in crossflow with a velocity ratio of 3.8 and $Re = U_{cf}D/\nu = 6600$ have been experimentally determined by pattern recognition of the velocity field measured with a rake of hot-wire anemometers at two downstream locations, $X = 5$ and 15. Results show that the dominant CVP, which is easily observed and detected in the mean velocity field, is not a steady feature of the jet in crossflow. Rather, the intensity of the two counter-rotating vortices fluctuates strongly, and this fluctuation is driven by the Kármán-like vortices present in the pseudo-wake that forms behind the jet. It should be noted that this wake is less periodic than the wake behind a circular cylinder, even near to the jet. Also, the pseudo-wake has a very small velocity defect because there is no boundary layer separation at the jet interface and, therefore, there is pressure recovery at horizontal planes located at 3 or 4 diameters from the wall. This weak periodicity of the wake and its relative weakness precluded the observation of its

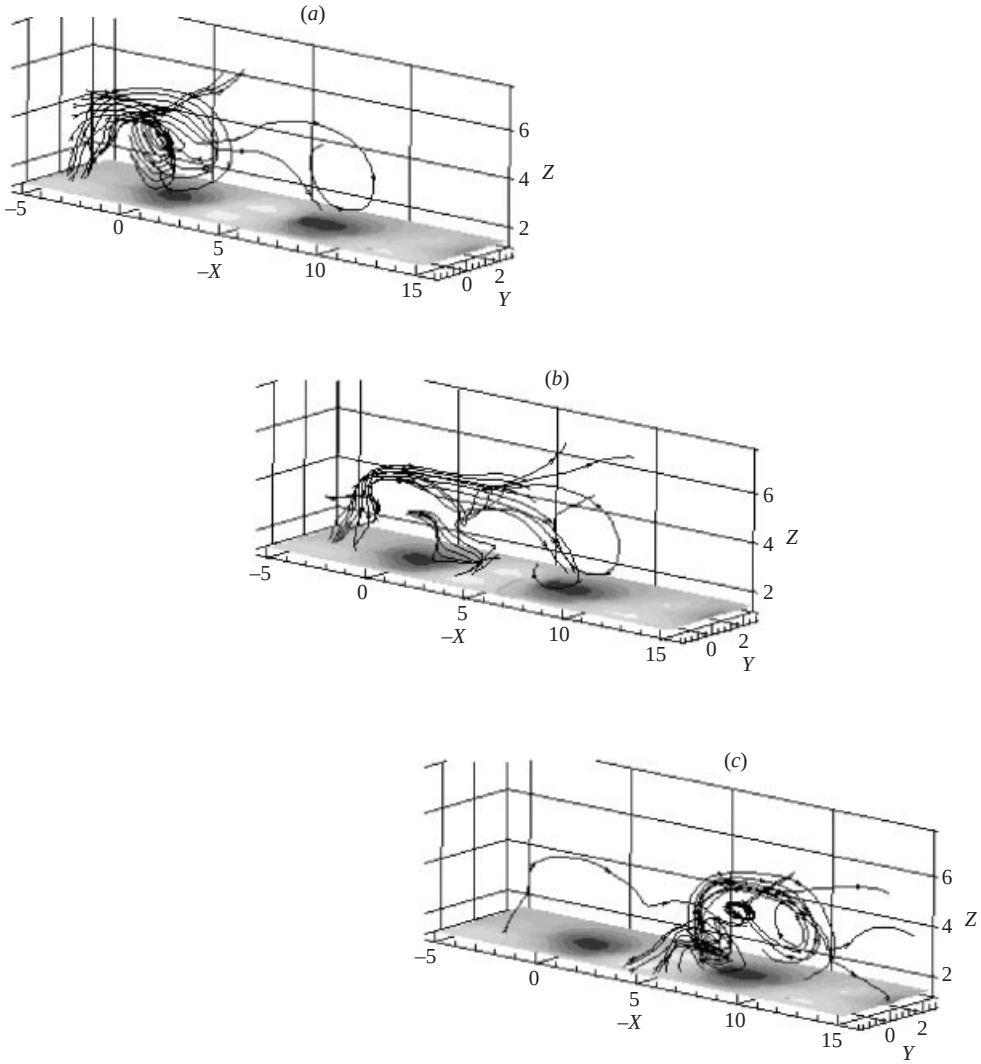

FIGURE 14. Three sets of streamlines in the three-dimensional total velocity field over the y-positive half of the jet as seen by an observer moving with a convection velocity equal to U_{cf}. Isocontours of V at $Z = 1.5$ identify lateral motions downstream of the jet exit.

connection to the jet structure until the visualization results of Fric & Roshko (1994). Moreover, it has not been until the application of the PR technique to hot-wire data, that the kind of structures detected by flow visualization have also been quantitatively measured by Eiff & Keffer (1997) and in the present work. The results reported here show that the coherent motions that ride over the CVP and modulate it, are not just slight fluctuations of these vortices, because their coherent vorticity attains even higher values than those of the vorticity contained in the CVP. A non-stationary structure identified as 'handle-type' vortices that link the vertical vortices in the wake with the CVP is responsible for the aforementioned modulation.

Figure 15 summarizes the structural characteristics of the jet in crossflow that stem from the interaction between the handle-type vortices and the CVP meandering

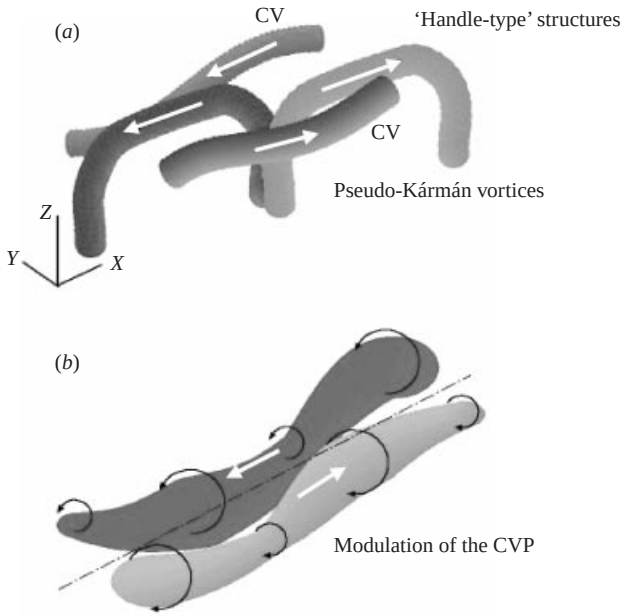

FIGURE 15. Sketch of the process of CVP modulation. (*a*) Handle-type structures superimposed to the $\pm\Omega_x$ vortex tubes of the CVP; (*b*) the amplitude modulated CVP.

pattern, which has been presented in figure 11 in terms of the time-evolution of Ω_x in a time sequence of vertical slices through the total vorticity field. Figure 15(*a*) presents a sketch of the process by which a pair of $\pm\Omega_x$ vortex tubes superimposed on handle-type structures yields a pair of intensity modulated vortices, i.e. the modulated CVP shown in figure 15(*b*). The rest of structures detected – horseshoe vortices in the wake and folded vortex rings – coincide with those investigated by Eiff & Keffer (1997) and Kelso *et al.* (1996).

Finally, figure 16 shows a sketch of all the structures present in the jet and in the boundary layer, drawn over one of the current instantaneous flow visualizations, and how they are linked to each other. The upstream lateral (y-direction) vorticity Ω_y in the wall boundary layer is lifted as the crossflow approaches the jet exit and senses the adverse gradient pressure imposed by the jet. This pressure field is also responsible for the generation of vorticity of opposite sign that forms near the wall at the upstream side of the jet and constitutes the front horseshoe vortex system. This horseshoe vortex system is not included in figure 15 for clarity. The azimuthal vorticity in the inner pipe walls is reoriented as the jet exits and penetrates the above-mentioned pressure field; the adverse pressure gradient at the upstream side slows down the associated vortex rings and the opposite occurs at the downstream side where the vortex is lifted. The overpressure both at the front and inside the jet exit is the main mechanism responsible for the distortion and reorientation of vorticity.

On the other hand, the fast homogenization of the pressure field from the exit plays an important role in the vortex breakdown that occurs on the downstream side of the jet, which results in small-scale turbulence production. Likewise, the alternate shedding in the leeward side of the jet is due to the lateral separation of the wall boundary layer giving place to the upright or Kármán-like vortices in the pseudo-wake that develops downstream of the jet. Therefore, the pressure field around the jet

FIGURE 16. Sketch over an instantaneous photograph of the significant vorticity lines and instantaneous structures currently identified in the jet in crossflow. The following are observed: the vortex lines in the wall boundary layer upstream of the jet; the vortex rings as they are folded and wrinkled; the vertical horseshoes from the bottom of the wall to the top of the upper jet interface; and finally the 'handle-type' structures, which are similar to the horseshoes, but located along the lower jet interface, where the cores of the CVP are placed.

exit plays a dominant role in the formation mechanism of the far-field structures. This role has been underestimated in most studies previously published in the literature. As the jet flows away from the exit, the initial conditions are very rapidly forgotten due to the strong process of 'tubularization' associated with the CVP and three structures remain, as shown in figure 15.

This work was supported by the 'Dirección General de Investigación Científica y Técnica' (Spain), project no. PB96-1011, and the 'Programa de Grups de Recerca Consolidats de la Generalitat de Catalunya', project no. 1998SGR-00102. A. Rivero was financially supported by Universitat Rovira i Virgili during the course of this investigation.

REFERENCES

ADLER, D. & BARON, A. 1979 Prediction of a three-dimensional circular turbulent jet in crossflow. *AIAA J.* **17**, 168–174.

ANDREOPOULOS, J. 1985 On the structure of jets in a crossflow. *J. Fluid Mech.* **157**, 163–197.

BLANCHARD, J. N., BRUNET, Y. & MERLEN, A. 1999 Influence of a counter rotating vortex pair on

the stability of a jet in a cross flow: an experimental study by flow visualizations. *Exps. Fluids* **26**, 63–74.

Broadwell, J. E. & Breidenthal, R. E. 1984 Structure and mixing of a transverse jet in incompressible flow. *J. Fluid Mech.* **148**, 405–412.

Coelho, S. L. V. & Hunt, J. C. R. 1989 The dynamics of the near field of strong jets in crossflow. *J. Fluid Mech.* **200**, 95–120.

Eiff, O. S., Kawall, J. G. & Keffer, J. F. 1995 Lock-in vortices in the wake of an elevated round turbulent jet in a crossflow. *Exps. Fluids* **19**, 203–213.

Eiff, O. S. & Keffer, J. F. 1997 On the structures in the near wake region of an elevated turbulent jet in a crossflow. *J. Fluid Mech.* **333**, 161–195.

Fearn, R. & Weston, R. P. 1978 Induced velocity field of a jet in a crossflow. *NASA TP*-1087.

Ferré, J. A. & Giralt, F. 1989 Pattern recognition analysis of the velocity field in plane turbulent wakes. *J. Fluid Mech.* **198**, 27–64.

Foss, J. F. 1980 Interaction region phenomena for the jet in a crossflow problem. *Rep.* SFB 80/E/161. Univ. Karlsruhe.

Fric, T. F. 1990 Structure in the near field of the transverse jet. PhD Thesis, GALCIT, California Institute of Technology.

Fric, T. F. & Roshko, A. 1994 Vortical structure in the wake of a transverse jet. *J. Fluid Mech.* **279**, 1–47.

Haven, B. A. & Kurosaka, M. 1997 Kidney and anti-kidney vortices in crossflow jets. *J. Fluid Mech.* **352**, 27–64.

Hussain, A. K. M. F. 1983 Coherent structures – reality and myth. *Phys. Fluids* **26**, 2816–2850.

Kamotani, Y. & Greber, I. 1971 Experiments on a turbulent jet in a crossflow. *NASA CR* 72893.

Karagozian, A. R. 1986 Analytical model for the vorticity associated with a transverse jet. *AIAA J.* **24**, 429–436.

Kawall, J. G., Shokr, M. & Keffer, J. F. 1983 A digital technique for the simultaneous measurement of streamwise and lateral velocities in turbulent flows. *J. Fluid Mech.* **133**, 83–112.

Keffer, J. F. & Baines, W. D. 1963 The round turbulent jet in a crosswind. *J. Fluid Mech.* **15**, 481–496.

Kelso, R. M., Lim, T. T. & Perry, A. E. 1996 An experimental study of round jets in a crossflow. *J. Fluid Mech.* **306**, 111–144.

Kelso, R. M. & Smits, A. J. 1995 Horseshoe vortex systems resulting from the interaction between a laminar boundary layer and a transverse jet. *Phys. Fluids* **7**, 153–158.

Kopp, G. A., Ferré, J. A. & Giralt, F. 1997 The use of pattern recognition and POD in identifying the structure of fully-developed free turbulence. *Trans. ASME: J. Fluids Engng* **119**, 289–296.

Krothapalli, A., Lourenco, L. & Buchlin, J. M. 1990 Separated flow upstream of a jet in a crossflow. *AIAA J.* **28**, 414–420.

Licinsky, D. S., True, B. & Holderman, J. D. 1995 Influence of initial conditions in jets in crossflow. *AIAA Paper* 95–2998.

Margason, R. J. 1993 Fifty years of jet in cross flow research. *AGARD CP*-534.

Morton, B. R. & Ibbetson, A. 1996 Jets deflected in a crossflow. *Expl Therm. Fluid Sci.* **12**, 112–133.

Pratte, B. D. & Baines, W. D. 1967 Profiles of the round turbulent jet in a cross flow. *J. Hydraul. Div., ASCE* **92**, 53–64.

Rivero, A. 2000 Estructuras coherentes y mezcla en un chorro inyectado en una corriente transversal. Doctoral thesis (in Spanish), Universitat Rovira Virgili, Tarragona, Spain.

Rudman, M. 1996 Simulation of the near field of a jet in a crossflow. *Expl Therm. Fluid Sci.* **12**, 134–141.

Schetz, J. A. 1980 Injection and mixing in turbulent flow. *AIAA J.* **68**, 145–164.

Smith, S. H. & Mungal, M. G. 1998 Mixing structure and scaling of the jet in crossflow. *J. Fluid Mech.* **357**, 83–122.

Smith, S. H., Lozano, A., Mungal, M. G. & Hanson, R. K. 1993 Scalar mixing in the subsonic jet in a crossflow. *AGARD CP*-534.

Sykes, R. I., Lewellen, W. S. & Parker, S. F. 1986 On the vorticity dynamics of a turbulent jet in a crossflow. *J. Fluid Mech.* **80**, 393–413.

Vernet, A., Kopp, G. A., Ferré, J. A. & Giralt, F. 1999 Three-dimensional structure and momentum transfer in a turbulent cylinder wake *J. Fluid Mech.* **394**, 303–337.

VERNET, A., KOPP, G. A. & GIRALT, F. 2000 Identification of critical points in a turbulent wake with fuzzy clustering. In *Turbulence, Heat and Mass Transfer 3* (ed. Y. Nagano, K. Hanjalic and T. Tsuji), pp. 621–628. Aichi Shuppan, Tokyo.

YUAN, L. L., STREET, R. L. & FERZIGER, J. H. 1999 Large eddy simulation of a round jet in a crossflow. *J. Fluid Mech.* **379**, 71–104.

ZAMAN, K. B. M. Q. & FOSS, J. K. 1997 The effect of vortex generators on a jet in a crossflow. *Phys. Fluids* **9**, 106–114.